

The Evolution of X-ray Clusters and the Entropy of the Intra-Cluster Medium

Paolo Tozzi¹

and

Colin Norman

Department of Physics and Astronomy, Johns Hopkins University, Baltimore, MD 21218.

ABSTRACT

The thermodynamics of the diffuse, X-ray emitting gas in clusters of galaxies is determined by gravitational processes associated with infalling gas, shock heating and adiabatic compression, and non-gravitational processes such as heating by SNe, stellar winds, activity in central galactic nuclei, and radiative cooling. The effect of gravitational processes on the thermodynamics of the Intra Cluster Medium (ICM) can be expressed in terms of the ICM entropy. The entropy is a convenient variable as long as cooling is negligible, since it remains constant during the phase of adiabatic compression during accretion into the potential well, and it shows a single step-like increase during shock heating. Observations indicate that non-gravitational processes also play a key role in determining the distribution of entropy in the ICM. In particular an entropy excess with respect to that produced by purely gravitational processes has been recently detected in the centers of low temperature systems. This type of entropy excess is believed to be responsible for many other properties of local X-ray clusters, including the $L-T$ relation and the flat density cores in clusters and groups.

In this paper we assume that the entropy excess is present in the Intergalactic Medium (IGM) baryons before the gas is accreted by the dark matter halos and reaches high densities. We use a generalized spherical model to compute the X-ray properties of groups and clusters for a range of initial entropy levels in the IGM and for a range of mass scales, cosmic epochs and background cosmologies. In particular, we follow the formation of adiabatic cores during the first stages of the gravitational collapse, and the subsequent evolution of the central entropy due to radiative energy loss. The model predicts the statistical properties of the cluster population at a given epoch, and also allows study of the evolution of single X-ray halos as a function of their age.

We find that the statistical properties of the X-ray clusters strongly depend on the value of the initial background entropy. Assuming a constant, uniform value for the background entropy, the present-day X-ray data are well fitted for the following range of values of the adiabatic constant $K_* \equiv k_B T / \mu m_p \rho^{2/3} = (0.4 \pm 0.1) \times 10^{34} \text{ erg cm}^2$

¹Osservatorio Astronomico di Trieste, via Tiepolo 11, I-34131 Trieste, Italy

$\text{g}^{-5/3}$ for clusters with average temperatures $kT > 2 \text{ keV}$; $K_* = (0.2 \pm 0.1) \times 10^{34} \text{ erg cm}^2 \text{ g}^{-5/3}$ for groups and clusters with average temperatures $k_B T < 2 \text{ keV}$. These values correspond to different excess energy per particle of $k_B T \geq 0.1 (K_*/0.4 \times 10^{34}) \text{ keV}$. The dependence of K_* on the mass scale can be well reproduced by an epoch dependent external entropy: the relation $K_* = 0.8(1+z)^{-1} \times 10^{34} \text{ erg cm}^2 \text{ g}^{-5/3}$ fits the data over the whole temperature range. The model can be extended to include internal heating, but in this case the energy budget required to fit the X-ray properties would be much higher. Observations of both local and distant clusters can be used to trace the distribution and the evolution of the entropy in the cosmic baryons, and to constrain the typical epoch and the source of the heating processes. The X-ray satellites Chandra and XMM can add to our knowledge of the history of the cosmic baryons, already derived from the high redshift, low density gas observed in the QSO absorption-line clouds, by imaging the hot, higher density plasma observed in groups and clusters of galaxies.

Subject headings: cosmology: theory – galaxies: clusters: general – hydrodynamics – X-rays: galaxies

1. INTRODUCTION

Clusters of galaxies are the largest virialized objects in the Universe, and are usually considered a canonical data set for testing cosmology. They are the largest collections of diffuse, highly ionized baryons that are directly observable in X-rays mostly through thermal bremsstrahlung emission. The strong dependence of X-ray emission on density $L \propto \rho^2$ allows one to select clusters and define complete samples much better than in the optical band.

X-ray observations of cluster number counts, luminosity functions and temperature distributions indicate little apparent evolution in clusters back to redshifts as high as ~ 0.7 (e.g., Henry 1997, 2000; Rosati et al. 1998; Schindler 1999), with the exception of very high luminosity objects or very high redshifts (Gioia et al. 1990; Rosati et al. 2000). This set of results provides one of the strongest challenges to high-density cosmological models in which cluster evolution is expected to be detectable even at redshifts as low as $z \simeq 0.3$. However, these tests are highly dependent on the thermodynamic evolution of the ICM (e.g. see Borgani et al. 1999 and references therein; Bower 1997). The best-fit cosmological parameters are degenerate with the phenomenological parameters used to describe the evolutionary properties of the ICM. In fact, the diffuse baryons in clusters do not simply follow the dark matter, as would be the case if they were driven only by gravity as in self-similar models (Kaiser 1986). Significant efforts have been devoted recently to building a physical model for the ICM including an energy scale at which baryons and dark matter effectively decouple and the self-similarity is broken.

The presence of a minimum entropy in the pre-collapse IGM has been advocated for some time as a way to naturally break the self-similar behaviour (Kaiser 1991, Evrard & Henry 1991). Such

an extra entropy is the key ingredient in reproducing the observed luminosity–temperature relation $L \propto T^n$ with $n \simeq 3$ (David et al. 1993, Mushotzky & Scharf 1997, Allen & Fabian 1998; Arnaud & Evrard 1999; Markevitch 1998), which is at variance with the self–similar prediction $L \propto T^2$. Such an entropy minimum bends the relation from self–similar $L \propto T^2$ behaviour at very large scales ($\sim 10^{15} M_\odot$) towards a steeper slope on the scale of groups ($\sim 10^{13} - 10^{14} M_\odot$) which is actually observed (Ponman et al. 1996; Helsdon & Ponman 2000). The average $L \propto T^3$ relationship is essentially produced by the flattening of the density distribution in the cores of the X–ray halos; such cores grow larger as the mass scale decreases, and the luminosity steepens further on the scale of groups, where the gas is only adiabatically compressed (see Balogh, Babul & Patton 1999; Cavaliere, Menci & Tozzi 1997, hereafter CMT97; Cavaliere, Menci & Tozzi 1999).

The picture has been reinforced by the net change observed in the chemical properties and the spatial distribution of the ICM on the scale of groups, below the observed temperature of 1 keV (Renzini 1997, 1999) where the effects of the entropy excess are expected to be strongest. Another piece of evidence can be obtained from the observed mass–temperature relation (see Horner, Mushotzky & Scharf 1999). Recently, an excess of entropy (with respect to the self similar scaling) has been directly detected in the central regions of small clusters with temperatures between 1 and 3 keV (Ponman, Cannon & Navarro 1999, hereafter PCN; see also Lloyd–Davies, Ponman & Cannon 2000), pointing to the role of the entropy as the key ingredient determining the different properties of clusters and groups.

Independent hints come from the extragalactic X–ray background: without a substantial entropy injection at early epochs, its level and correlation function would exceed the observed limits, due to the widespread cooling phenomena that would radiate most of the gravitational energy of the collapsing baryons in the soft X–ray band (Pen 1999; Wu, Fabian & Nulsen 1999).

However, even if there are many hints pointing towards a comprehensive picture, there is a large uncertainty on the amount of extra–energy that effectively generates the entropy excess. It can be shown that it is the final entropy distribution that determines both the spatial distribution of the ICM and its evolutionary properties, irrespective of the total energy released in the past. A given entropy level can be reached through different thermodynamic histories, so that it is not possible to relate the ICM properties directly to a given energy excess without knowing the detailed physics of the heating processes. As we will show in this paper, the first question to answer is not: *how much energy has been released in the ICM?* but rather: *what is the sequence of adiabats through which the baryons evolve?*

It is difficult to predict *a priori* the entropy excess of the cosmic baryons, since most of the processes regulating nuclear activity, star and galaxy formation, and the transfer of energy to the surrounding baryons, are out of reach of present–day techniques. Thus, at present there is no general consensus on the production mechanism of such extra–entropy. For example, it is not clear whether the entropy minimum has been established in the IGM before it has been accreted –the external scenario, or in the high density ICM after accretion–the internal scenario. A different

energy budget is required in the two different scenarios: a few tenths of a keV per particle are needed if the entropy is generated early enough to keep the baryons on a high adiabat, which prevents them from reaching high densities and cooling massively; much higher energy excess (> 1 keV per particle) is required if the entropy is generated later, when the cooling process is eventually already widespread and most of the gas is already at high densities (Tozzi, Scharf & Norman 2000, hereafter TSN00).

The external scenario, which we will assume as a reference model, is provided by a ubiquitous entropy *floor* in the diffuse gas, which is entirely due to non-gravitational processes and is assumed to be in place before the onset of gravitational collapse of massive halos. The initial extra entropy is ineffective in large mass systems, where most of the entropy is due to strong shocks, but is more important in smaller mass systems, where the entropy production via shocks is strongly reduced. Eventually a large part of the baryons are merely adiabatically compressed and retain full memory of the initial entropy level. The non-gravitational origin of the excess entropy is crucial, since its level is independent of the mass scale and it breaks the self-similarity, while gravitational processes always scale self-similarly with mass.

We present a detailed model to relate the thermodynamic properties of the ICM in groups and clusters of galaxies to an initial entropy excess in the IGM, taking into account the transition between the adiabatic and the shock regime in the growth of X-ray emitting halos. The effect of radiative cooling is also included. We show that, despite the many complexities involved, the entropy is always a convenient synthetic quantity to describe the thermodynamic history of the cosmic baryons at least on the scale of groups and clusters. In particular, we show that in many circumstances the entropy track of a shell of baryons being accreted onto dark matter halos goes through three major regimes: (1) adiabatic compression, during which both heating and cooling are negligible and the entropy is constant; (2) step-like discontinuities due to gravitationally induced shocks; and (3) slow decrease when cooling becomes efficient for baryons in the inner regions of large halos. The entropy jump, the onset of cooling, and the final spatial distribution of the ICM, depend on the initial entropy. Such an external, initial entropy level can be reconstructed from the observation of a large number of distant clusters, or from the spatially and spectrally resolved profiles of nearby halos (see TSN00). Even if the knowledge of the entropy does not resolve the details of the underlying heating history and determine unambiguously the energy budget, the combination of data in the X-ray band with data in the optical and infrared bands can help to identify the major source of heating. In principle, this allows a detailed reconstruction of the energetic processes that affect the cosmic baryons over a wide range of scales and cosmic epochs.

The paper is organized as follows. In §2 we establish a one-to-one correspondence between the entropy level and the distribution of the ICM in halos in equilibrium. In §3 we present a generalized spherical infall model to follow the entropy track of each shell. In §4 we derive the average density and temperature profiles and the related global properties such as luminosity, emission weighted temperature and core radius, as a function of mass scale, cosmology, epoch and dark matter profile. In §5 we widen the parameter space, and investigate a time-dependent background entropy to show

how the evolution in the entropy reflects in the X-ray properties of clusters of galaxies. In §6 we discuss the limitation of the present approach. Finally, our conclusions and future perspectives are presented in §7.

2. ICM THERMODYNAMICS: ENTROPY

The position, density and temperature of each shell in hydrostatic equilibrium in a given dark matter halo (whose average properties are determined by its total virialized mass M_0 at the epoch of observation z_0), can be unambiguously recovered once the final entropy profile is known. Assuming a spherical mass distribution, the equation of hydrostatic equilibrium for diffuse baryons in the potential well is:

$$\frac{1}{\rho} \frac{dp}{dx} = -C \frac{m(< x)}{x^2}, \quad (1)$$

where the radius x , the pressure p and the density ρ refer to the baryons and are normalized to the respective values at the last accreted shell at $z = z_0$, while m is the total mass profile normalized to the total virialized mass. Explicitly, $x \equiv R/R_s$, $p \equiv P/P_s$, $\rho = \rho_B/\rho_s$, and $m(< x) \equiv M(< x)/M_0$. Since dark matter and baryons are distributed differently, we write $M(< x) = M_{DM}(< x) + M_B(< x)$. The constant is $C = -GM_0\mu m_p/R_s k_B T_s$, where m_p is the proton mass, G is the gravitational constant, k_B is the Boltzmann constant and μ is the molecular weight of the plasma (we will assume $\mu \simeq 0.59$ for a primordial IGM). T_s is the temperature of the last accreted baryonic shell. In the following we will refer to the values of the last accreted shell as the shock value, even in the limit of a vanishingly small shock. We assume that hydrodynamic equilibrium is instantaneously established after each accretion event.

We define the adiabat $K \equiv k_B T / \mu m_p \rho_B^{\gamma-1}$ (following the notation of Balogh, Babul & Patton 1999), where $S \propto \ln(K)$ is the entropy and γ is the microscopic adiabatic index which is $\gamma = 5/3$ for a monoatomic gas. Using the perfect gas equation, we can write the density in terms of pressure and entropy normalized to the value at the last accreted shell, with each shell scaled to the corresponding adiabat: $\rho = p^{1/\gamma} k^{-1/\gamma}$, where $k \equiv K(x)/K_s$. Substituting in Equation (1), the equilibrium pressure profile is re-written as:

$$\frac{dp}{dx} = -C p^{1/\gamma} k^{-1/\gamma} \frac{m(< x)}{x^2}. \quad (2)$$

The above expression allows us to calculate the thermodynamic properties of a hydrostatic distribution of gas when the adiabat profile $K(x)$ is known. The main difference from the usual solutions of the hydrostatic equilibrium equation is that there is no need to assume a polytropic index, since each shell already sits on its adiabat which is determined by its previous history, and the correspondence between density and temperature is unambiguous.

The problem reduces to finding the proper adiabat of each infalling shell, or the entropy as a function of the accreted baryons, since the baryonic mass included in a given shell is constant

with time. This procedure is convenient when applied to clusters of galaxies, because the entropy is conserved for the majority of the time. In fact, the dynamic history of a shell of gas can be described in three steps: 1) adiabatic compression during the infall; 2) shock heating at the accretion; 3) compression within the potential well due to further growth of the halo. The entropy is therefore constant during the first and third phase, and the jump at the shock is the most important feature needed to reconstruct the final profile. Cooling introduces further complexity, because for the inner, higher density shells, the radiative loss becomes important, changing substantially the final adiabats with respect to the initial value. However, as we will see later, the cooling can be included in the above picture, as long as the initial adiabat is not too low.

To begin with, we focus on the most important event in the entropy history of each shell: the accretion epoch. To calculate the value of K immediately after the accretion shock, we need to estimate both the density and the temperature of each shell after shock heating eventually raised the adiabat from the external value to the post-accretion value $K_t(x)$. If a shock does not occur, the baryons are only adiabatically compressed and are accreted with the same adiabat. To determine whether a shell is shocked or not during accretion, we build a spherical infall model for the baryons, generalized for different cosmologies and epochs.

3. A GENERALIZED SPHERICAL MODEL

In the framework of the hierarchical clustering scenario, the baryons are accreted along with the dark matter during the process of gravitational collapse. An expanding accretion shock at the interface of the inner hydrostatic gas with a cooler, adiabatically-compressed, external medium, located approximately at the virial radius of the cluster, is a longstanding prediction from such gravitationally-driven models (see the 1D models of Bertschinger 1985, Ryu & Kang 1997, Knight & Ponman 1997, Takizawa & Mineshige 1998, and the 3D numerical simulations of Evrard 1990, Roettiger et al. 1993, Metzler & Evrard 1994, Bryan & Norman 1998, Abadi, Bower & Navarro 2000). Due to the growth of the total virialized mass, the baryons accreted later experience larger shocks, and the resulting entropy profile is always growing outwards. Such gravitationally-driven models predict X-ray properties which scale self-similarly with mass and fail to reproduce the X-ray observations of clusters.

A non-negligible value of the background entropy is needed in order to break the self-similarity. In fact, an initial adiabat will prevent shocks occurring below a given mass scale. We now discuss the external scenario in which an initial adiabat K_* is imprinted on all the diffuse IGM at some epoch prior to the formation of the dark matter potential wells. We refer to K_* as to the background entropy established in the IGM by non-gravitational processes before the baryons are accreted.

3.1. Accretion and Shock Conditions

The most prominent feature of the entropy history of each shell is the discontinuity at the accretion shock. To calculate the discontinuity we need to know the pre-shock density and the temperature that the infalling gas reaches moving along the initial adiabat K_* before accretion. Then we calculate the postshock temperature and density using mass, momentum and energy conservation, in the limit of complete thermalization of the kinetic energy of the gas.

The first important quantity is the infall velocity v_i . The dependence of v_i on the total mass enclosed by the shell can be written as:

$$\frac{v_i^2}{2} = \frac{v_{ff}^2}{2} + \Delta W - \frac{c_s^2}{\gamma - 1} + \frac{c_s^2}{\gamma - 1} \left(\frac{\rho_{ta}}{\rho_e} \right)^{\gamma-1}, \quad (3)$$

where ρ_{ta} is the density at turnaround, ρ_e is the gas external density, $c_s = \sqrt{\gamma K_* \rho_e^{\gamma-1}}$ is the sound speed (hereafter $\gamma = 5/3$), both calculated at the accretion radius R_s , and v_{ff} is the free-fall velocity of a particle containing always the same amount of mass during the infall. Equation 3 is a generalized version of the Bernoulli equation for an adiabatic, spherically symmetrical accretion (Bondi 1952). The last quantity can be written as:

$$\frac{v_{ff}^2}{2} \equiv \frac{GM}{R_s} - \frac{GM}{R_{ta}}, \quad (4)$$

where M is the total mass initially included by the baryonic shell. The term ΔW is the contribution added to $v_{ff}^2/2$ to obtain the total work done by the gravitational potential on the baryonic shell, from the turnaround radius, R_{ta} , to the accretion radius R_s , including the effect of the time-varying enclosed mass. To evaluate this term it is strictly necessary to solve the trajectory of each baryonic shell. However we can make the simplifying assumption that the amount of dark matter enclosed by each shell, is a monotonically growing function of time, from the mass enclosed at turn around, to the final mass enclosed at the shock radius. The term ΔW is estimated in §A, and the uncertainty on it turns out to be approximately 10–30 %. We show later that this error is not important in determining the transition scale between the shock and the adiabatic regime.

The other two terms proportional to c_s^2 describe the energy needed to compress the gas. In fact, due to the non-negligible value of K_* in the infalling IGM, part of the gravitational energy goes into internal energy in an amount proportional to the square of the sound speed in the external IGM at the epoch of accretion, so that in general $v_i < v_{ff}$. The compression term carries an increasing fraction of the potential energy when the mass of the system is lower, or, since the sound speed is proportional to $K_*^{1/2}$, when the entropy is higher. The fourth term on the right hand side of Equation (3) results from the initial condition $v_i = 0$ for a gas shell at the turnaround radius, when the gas had a density ρ_{ta} and it is assumed to be at the same contrast of the dark matter. The epoch of turnaround is assumed to be half of the infall epoch.

Of course to solve Equation (3) we need to evaluate ρ_e . To do this, we first note that the knowledge of both the external density and the infall velocity gives the net infall accretion rate of

baryonic matter through the surface defined by the shock radius. Then, we make the assumption that *the growth rate of the total virialized mass \dot{M} is proportional to the growth rate of the thermalized baryonic mass \dot{M}_B* . Here \dot{M} is the average total mass accretion rate as predicted in the hierarchical clustering scenario. This means that all the baryons, that initially were in the same lagrangian volume of the mass that is currently virialized, have been accreted. The proportionality constant is simply the average mass fraction of baryons in diffuse form f_B , so that at each epoch the fraction of accreted baryons (with respect to the total baryons accreted at $z = z_0$), is equal to the fraction of the accreted matter to the total virialized mass at the same final epoch. This does not imply that the baryons are in the same volume; they are distributed in a volume typically larger than that of the accreted dark matter. This occurs especially in the adiabatic regime, when the baryons have too high a temperature to sink into the potential well and thus the accretion radius is significantly larger than the virial one. The constraint on the mass accretion rate translates into the relation:

$$\dot{M}_B = f_B \dot{M} = \rho_e 4\pi R_S^2 \left(v_i + \frac{dR_S}{dt} \right), \quad (5)$$

where \dot{M} is given for a particular cosmological model (see §3.3). We can derive ρ_e as a function of v_i , and then the external temperature is $k_B T_e = \mu m_p K_* \rho_e^{2/3}$.

The condition $v_i > c_s$ determines if the shell is shocked. In the frame of the infalling gas the shock expands with a velocity $v_i + dR_S/dt$. In the case of a shock, we assume that all the kinetic energy of the infalling gas is thermalized (i.e., the post-shock velocity $v_{ps} = 0$ in the rest-frame of the cluster), and obtain for the postshock temperature (Landau & Lifshitz 1957; Cavaliere, Menci & Tozzi 1998):

$$k_B T_i = \frac{\mu m_p v_i^2}{3} \left[\frac{(1 + \sqrt{1 + \epsilon})^2}{4} + \frac{7}{10} \epsilon - \frac{3}{20} \frac{\epsilon^2}{(1 + \sqrt{1 + \epsilon})^2} \right], \quad (6)$$

where $\epsilon \equiv 15k_B T_e / 4\mu m_p v_i^2$.

The postshock density is then $\rho_i = g \rho_e$, where g is the shock compression factor which depends on the postshock temperature, T_i , and the external temperature, T_e , and is given by (see CMT97):

$$g = 2 \left(1 - \frac{T_e}{T_i} \right) + \left[4 \left(1 - \frac{T_e}{T_i} \right)^2 + \frac{T_e}{T_i} \right]^{1/2}. \quad (7)$$

If the gas is shocked, we calculate the new adiabat $K_i = k_B T_i / \mu m_p \rho_i^{2/3}$ of the baryonic shell after accretion. If the infalling velocity is smaller than the sound speed in the external IGM and the shock does not occur, the gas is accreted adiabatically, and therefore the post-accretion adiabat is the initial one $K_i = K_*$, which is all we need to solve for the final equilibrium.

Thus, using Equations (3), (6) and (7), we are able to associate with each shell, including a mass M_B of baryons, its postshock adiabat $K_i(M_B)$. For a given object, the adiabat of the infalling shells initially will be $K_i = K_*$, since for sufficiently low velocities the shocks are suppressed. As the total mass grows, the velocities of the infalling shells rise approximately as $v_i \propto M^{1/3}$, more rapidly than the sound speed (which in general decreases with epoch, since $c_s \propto \rho_e^{1/3} \propto 1 + z$), and

eventually a shock regime begins. In Figure 1 the transition between the two regimes is shown as a function of the accreted mass for a given initial adiabat K_* . As it is shown in the first panel, the maximum uncertainty in the infalling velocity, v_i , grows toward the adiabatic regime, but it does not introduce a large error in the transition scale, since the infall velocity falls steeply below c_s . The rapid increase of both the infall and the free-fall velocity at the transition, occurs because the gravitational energy becomes sufficient to overcome the pressure support, and the accretion radius moves from a relatively distant position to a position very close to the virial radius. Clearly, the presence of a larger K_* further delays the onset of the shock heating regime, inhibiting adiabatic accretion for the majority of the baryons, especially in small mass systems.

At this stage, if we neglect further changes in the entropy, the adiabat in the final position is simply $K(x) = K_i$ and the Equation (2) can be solved easily without any further steps. However, for the inner shells, radiative cooling becomes important and the calculation of the final adiabat requires solving Equation (2) at different epochs, as explained in the following subsection.

3.2. The Effect of Radiative Cooling

Each shell of gas is continuously changing its adiabat due to cooling and heating processes. In particular, the first baryonic shells that are accreted drain into the inner, higher density regions of halos as the total virialized mass grows, and their cooling times become small enough to start cooling processes. As a result, the final adiabat of these baryonic shells will be lower than that at the accretion epoch, and eventually part of the gas leaves the diffuse, emitting phase and sinks into the center.

We can model the cooling assuming a homogeneous, single temperature distribution (Fabian & Nulsen 1977, Mathews & Bregman 1978); in this case the energy equation can be formally written as:

$$\frac{d}{dt}[\ln(K)] = -\frac{1}{\tau_{cool}(K)}, \quad (8)$$

where the cooling time τ_{cool} is defined as:

$$\tau_{cool} \equiv \frac{3}{2} \frac{k_B T}{\Lambda_{net}} \frac{\rho_B}{\mu m_p}, \quad (9)$$

and therefore it depends on K through T , ρ_B and Λ_{net} . Here Λ_{net} is the cooling rate including free-free and line emission (see Sutherland & Dopita 1993).

It is well known that cooling is a runaway process, and the solution of Equation (8) would require the computation of the equilibrium profile at many different epochs. Since we still want to have the benefit of a relatively fast computation, much faster than a full hydrodynamic simulation, we tackle the problem choosing a medium resolution in time ($\Delta t \simeq 0.3$ Gyr) and solving Equation (8) within Δt for every shell with an analytic approximation. This is possible if we assume that the cooling process is isobaric within Δt , in order to express both density and temperature as a

function of the adiabat K only. The pressure is updated at each time step, following the new equilibrium configuration. An intermediate step is to approximate the cooling function, Λ_{net} , with an analytic function of the temperature. In this way the change in the adiabat within Δt can be derived as the integral of an analytic function, as described in Appendix §B.

When the cooling times become very short in the center of the halo, part of the gas may eventually cool in a single time step Δt (i.e., its entropy drops to zero). In this case, the gas is removed from the diffuse, emitting phase, and is included in a gravitational term as if it is all accumulated in the very center. At this level, we do not implement more sophisticated multiphase models which can be important for the detailed emissivity distribution in cooling flows. However, we can follow the steepening of the baryonic density in the center as the radiative cooling becomes efficient, and compute the corresponding amount of baryons which drop out from the diffuse phase. We stress the fact that we are able to follow the complex cooling processes with good accuracy by virtue of the initial entropy level. The background entropy, in fact, delays and possibly inhibits the onset of strong cooling flows. Our model breaks down in the limit of small initial entropy, where the cooling catastrophe occurs.

The evolution of the adiabat as a function of cosmic epoch for some given shells is plotted in Figure 2. The outermost shells are accreted at later epochs. They are strongly shocked and reach a high adiabat, and find equilibrium at large radii and low densities. Consequently, the cooling times are always large and the adiabat K stays almost constant after the accretion. Conversely, inner shells are more affected by cooling for two reasons: they reach much higher densities (being in the central regions), and they have more time to cool since they are accreted much earlier. Eventually, the very inner shells reach very low entropy, corresponding to extremely high densities and very short cooling times, and they rapidly cool and drop out of the diffuse phase.

The calculation without the inclusion of cooling would be much simpler, since the final adiabat would be the accretion value K_i for all the shells, and the hydrostatic equilibrium would be solved only once (at the final epoch z_0). However, solving the equilibrium at several epochs allows us to follow the evolution of the X-ray properties for each (average) dark matter halo. In Figure 3 the evolution of temperature and luminosity for three objects of $10^{15}h^{-1}$ (continuous line), $10^{14}h^{-1}$ (dashed line), and $10^{13}h^{-1} M_\odot$ (dotted line), is shown for a constant $K_* = 0.3 \times 10^{34} \text{ erg cm}^2 \text{ g}^{-5/3}$ in a Λ CDM cosmology. In the third panel, the time evolution of the shock radius is plotted for the same objects. The shock radius is normalized to the virial radius at each epoch. It is possible to see how the shock radius is close to the virial one for the largest halo and relaxes in the last few Gyr when the mass accretion slows down and the external pressure term correspondingly decreases. The effect is more pronounced at lower masses, where the internal pressure support is strong enough to dominate the gravitational potential and the external pressure term of the infalling gas.

In Figure 4 we plotted, for the same three final masses, some relevant quantities averaged over the adiabatic cores, defined as regions including the gas accreted during the adiabatic regime. It is possible to see how the initial entropy $K_* = 0.3 \times 10^{34} \text{ erg cm}^2 \text{ g}^{-5/3}$ introduces a large difference

in the central core as a function of mass. Central densities are much higher for deeper potential wells. In addition, the baryons in the center of massive clusters suffer radiative losses and the baryonic cores shrink to smaller sizes and higher densities. In the second panel the average entropy of the inner cores is shown. The decrease due to the radiative cooling can reduce the initial entropy especially in the most massive halo. The decrease in the entropy is driven by the decrease in the average cooling time shown in the third panel. While the entropy is decreasing, the internal energy of the gas is still rising due to the compressional work done by the gravitational potential. However, the trend of stronger cooling for larger masses, is reversed in the case of very small K_* . In fact, as long as there is nothing to prevent the baryons from cooling, the amount of radiative losses is mainly set by the age of the halos.

3.3. Dark Matter Properties

In this section we briefly review the properties of the dark matter halos which drive gravitationally the evolution of the diffuse baryons. In particular we describe the mass profiles and the mass accretion rates in the framework of the hierarchical clustering scenario in universes dominated by cold dark matter (CDM). However, the model can be generalized to other cosmologies.

The boundary of a halo is the virial radius, defined as the radius within which the average overdensity with respect to the critical density is Δ_c , where $\Delta_c = 178$ for $\Omega_0 = 1$ with a mild dependence on Ω_0 (see, e.g., Eke et al. 1998). Analytical studies indicate simple power law profiles for the dark matter, of the kind $\rho \propto x^{-\xi}$, with $\xi = 9/4$ (Gunn & Gott 1972, Bertschinger 1985). Numerical works show a more complex behaviour, with a characteristic internal scale radius that depends on the epoch and on the final mass (Navarro, Frenk and White 1997, hereafter NFW; Moore et al. 1998). A very general expression for the universal profile is:

$$\rho = \rho_{c0} \frac{\delta_c}{(cx/x_v)^\nu [1 + (cx/x_v)^\zeta]^\eta}, \quad (10)$$

where c is the mass dependent concentration parameter of the dark matter, and δ_c is defined by requiring the average density within R_V with respect to the critical density to be Δ_c . Here we used $x_v \equiv R_v/R_s$ to be consistent with Equation (2) where the radius is normalized to R_s . Present calculations differ mainly in the inner regions, where NFW predict $\nu = 1$, $\zeta = 1$ and $\eta = 2$, while Moore et al. (1998) have a steeper inner profile with $\nu = 1.5$, $\zeta = 1.5$ and $\eta = 1$. From Equation (10) the mass profiles $m(< r)$ entering Equation (2) follow directly.

We will approximate the concentration parameter with power laws, which turn out to be good approximations (Navarro et al. 1997). The expressions used are described in appendix §C. In general, the concentration parameter c depends on the characteristic epoch of formation of the halo, which in turn depends on cosmology, perturbation spectrum, M_0 and z_0 (see NFW). This is because the dark matter *remembers* the epoch when each shell was accreted, even if the shell-crossing tends to erase such dynamical memory. For example, in a standard CDM universe groups

tend to have a larger concentration ($c \simeq 8$) being formed at higher epochs when the average density was higher, while clusters, being younger, have a lower concentration ($c \simeq 6$). At higher redshifts the concentration parameters are generally lower, since the difference in epoch (and thus in typical density) between formation and the observation epochs z_0 is reduced. These trends will be included in our calculations.

The accretion processes in groups and clusters show considerable scatter, as observed in numerical simulations and Monte Carlo realizations of hierarchical clustering based on the extended Press & Schechter formula (hereafter PS, Press & Schechter 1974, Bond et al. 1991, Bower 1991, Lacey & Cole 1993). However we are interested in the mass history of *typical* halos, each of them labeled by the final mass M_0 and the final (observation) epoch z_0 , for a given cosmology. The natural way to proceed is to average over many realizations of the mass history of the *main progenitor*, defined as the most massive halo participating in every mass accretion event along the merger tree of a single object. We run 1000 Monte Carlo simulations of the mass history of the main progenitor for different final masses M_0 and different final redshifts z_0 ($z_0 = 0$ and $z_0 = 1$) in the two cosmologies discussed below (tCDM and Λ CDM). We find that the average mass growth of the main progenitor can be approximated within few percent by a parabola in the $\log(m)$ – $\log(1+z)$ space:

$$m(z) = \left(\frac{1+z}{1+z_0} \right)^{-[B+A \log(\frac{1+z}{1+z_0})]}, \quad (11)$$

where A and B depend on cosmology, M_0 and z_0 . The relation (11) is used to determine the accretion epoch of each baryonic shell after Equation (5), and thus to compute its density, ρ_e , at the accretion shock.

The dispersion in the profiles and in the accretion process is likely to introduce some dispersion in the resulting X-ray properties, and is expected to explain partially the intrinsic scatter observed in the L – T relation. The intrinsic scatter in the emission is certainly due also to the presence of cooling flows (Allen & Fabian 1998; Arnaud & Evrard 1999), which in turn can be affected by both the dynamical and the heating history of the gas. For these reasons, we focus on typical halos averaging over many different realizations, and considering the accretion of baryons as a smooth and continuous process. These assumptions clearly break down in the case of massive merger events (see discussion in §6).

4. RESULTS

Here we present the X-ray properties of groups and clusters of galaxies in the case of a constant and homogeneous K_* in the external IGM. Our reference calculation will be a flat, low density cold dark matter universe (Λ CDM), which is currently preferred on the basis of the measurements of the expansion rate of the universe from high z SNe (Riess et al. 1998), from the Cosmic Microwave Background (see Lange et al. 2000; Balbi et al. 2000) and of the observation of a high baryonic fraction $f_{obs} > 0.06h^{-1.5}$ in clusters (see Ettori & Fabian 1999), which is consistent

with standard nucleosynthesis if $\Omega_0 < 0.3$ (White et al. 1993). The baryonic density is assumed to be $\Omega_B = 0.02h^{-2}$ (Burles & Tytler 1999a, 1999b), consistent with the standard primordial nucleosynthesis scenario. From the diffuse, X-ray emitting component, we exclude a fraction which is assumed to be locked in stars since the beginning, and is chosen to be 20 % of the total baryons in halos (independent of the mass scales and epoch, i.e., we assume a constant efficiency of star formation). The fraction of baryons cooled in the center, instead, is computed at each epoch and subtracted from the diffuse, X-ray emitting phase. For comparison, we will also discuss a tilted cold dark matter universe (tCDM), where we are forced to adopt a baryonic density $\Omega_B = 0.04h^{-2}$, larger than the standard value, in order to be consistent with the observed baryonic fraction. The details for the two universes are shown in Table 1. The values for A and B in the two universes are determined with a χ^2 fitting of the average mass histories with the relation (11), and are reported in Table 2.

4.1. Density and Temperature Profiles

First, we discuss a simple case where the cooling is not included, so that the final adiabat $K(x)$ is equal to the value at the accretion, K_i . This case shows the effects of the entropy excess alone without the intervention of cooling processes. In Figure 5 we show the resulting profiles for Λ CDM at redshift $z_0 = 0$, for an initial $K_{34} = 0.3$, where K_{34} is K_* in units of 10^{34} erg cm 2 g $^{-5/3}$. This value corresponds to a temperature $k_B T_* \simeq 1.5 \times 10^{-2}(1+z)^2$ keV at the ambient density. The dark matter is distributed according to the NFW profile. Three final masses are shown: $M_0 = 10^{15} - 10^{14} - 10^{13} h^{-1} M_\odot$. The plotted profiles are all normalized at the corresponding shock values in order to show how the scaling behaviour departs from self-similarity. Note, however, that the density and temperatures values at the shock in physical units are very different in the three cases.

A characteristic feature is the flat density profile of isentropic gas in the core, which is relatively larger at smaller masses (dashed lines in Figure 5, panel a). Such cores are built in the initial, high redshift stages of the accretion process, when the accretion is adiabatic since the infall velocities are small and shocks do not occur. This regime is relatively more extended going to lower masses. The pressure is more effective in pushing the baryons over a region larger than that of the dark matter (panel c). All this information is synthesized in the entropy profiles: at larger radii the entropy rises since the outer shells experience stronger shocks (panel d). Since the entropy is normalized to the value at the shock radius, the constant entropy floor in the center appears different at different masses. The slope of the entropy profile in the shock dominated regime is almost independent of the initial value K_* , yielding $d\ln(K)/d\ln x \simeq 1.1$; this value is close to the value 1.3 expected for the simple case of an isothermal profile where the entropy is due only to shock heating and $M_B \propto r$. The sharp knee in the entropy profile is due to the fact that the transition from adiabatic accretion to strong shocks is very fast, and the intermediate shock regime virtually does not exist, so that during the shock regime the entropy is always dominated by shock heating. In contrast, in the

center, isentropic cores are clearly emerging. The ratio of mass accreted adiabatically to the total baryonic mass, is correspondingly larger at lower mass scales (panel e).

Here we note that a departure from a power-law behaviour for the entropy profile has been observed in hydrodynamical simulations where neither radiative cooling nor extra-entropy were included (see Frenk et al. 1999). This may suggest that departures from a power-law behaviour in the entropy profile can also be originated by asphericity.

The temperature profiles (panel b) do show mild gradients in the regions where the gas has been shocked (variation less than a factor of 3 between R_s and $0.1R_s$), while they show considerable gradients when the entropy is constant, following $T \propto K_* \rho^{2/3}$. Part of the large gradient in the smallest system corresponds to very low luminosity regions, where the gas is relaxed due to the very small pressure term. These regions, and the corresponding large temperature gradients, have never been observed. In fact, if we compute the temperature gradient in the inner regions of halos with $M_0 = 10^{13} h^{-1} M_\odot$, we find an increase of about 2 within a radius of $0.1R_S \simeq 100 h^{-1}$ kpc, an effect hardly visible, e.g., in the data by ROSAT.

A good quantity to characterize the properties of the temperature profile is the effective polytropic index defined by the relation $p \propto \rho^{\gamma_p}$. In general, a family of polytropic relations can be used to describe the ICM and investigate the energy budget underlying each polytropic family (Loewenstein 2000). As a result of the combined action of shock heating and adiabatic compression, the index γ_p is found to be approximately $\gamma_p \simeq 0.8 - 1.2$ between the adiabatic core and the shock radius, roughly consistent with an isothermal temperature profile (in the Figure we show the value of γ_p averaged over $\Delta \log(x) = 0.3$). In the adiabatic cores the polytropic index is simply $\gamma_p = \gamma = 5/3$, since all the gas is on the same adiabat.

To elucidate how the breaking of self-similarity occurs, in Figure 6 we show the same profiles for a negligible value of the external entropy, but without the inclusion of cooling. This is what we call the self-similar case, which is different from the more realistic case of negligible entropy and the inclusion of cooling, since cooling also alters the entropy profile, as shown in §4.4. In the absence of an entropy floor, the profile $K(x)$ always decreases at smaller radii, and exhibits a power law behaviour without any particular scale. The only differences between groups and clusters are now driven by the dark matter distributions. Despite the pressure support, the gas essentially follows the dark matter, and groups appear more concentrated than clusters, reversing the trend of Figure 5.

In the $K_* \simeq 0$ case the cooling starts very early and deeply affects the profiles of massive clusters. The majority of the initially diffuse baryons cool in the center of small halos, where, without an effective background entropy, nothing prevents the baryons from cooling and the luminosity is dominated by the central regions. The cooling selectively removes the lower entropy gas in the center of lower mass objects, helping to create an entropy plateau at the very center, but with the entropy entirely produced by gravitational processes. This mechanism to create an entropy plateau has been advocated by PCN but a large amount of cooled baryons need to be accommodated in the

center. The strongest evidence for the presence of a background entropy at high z , is given by the low fraction of baryons in stars with respect to the total baryons available, which implies a strong suppression of the cooling processes especially in low mass halos (see Prunet & Blanchard 1999).

Figure 7 shows the case with $K_{34} = 0.3$ and with the inclusion of cooling. This case can be considered a realistic, complete scenario. As we shall see later, this value of the background entropy gives a good fit to the L – T relation. The inclusion of cooling introduced some change with respect to Figure 5, especially in the very inner regions, where the entropy evolved towards lower values. However the entropy excess in the center is still present (panel d). Cores with constant density appear more peaked, but small groups still show much flatter density profiles with respect to large clusters. The temperature profiles are lower, and the polytropic index γ_p is rapidly decreasing in the center.

For a more comprehensive view, the differences in the density profiles can be expressed in terms of fitting parameters β and r_c after adopting a beta model (Cavaliere & Fusco Femiano 1976). The results are shown in Figure 8. The β_{fit} parameter is about $\simeq 0.8$ in Λ CDM at $z = 0$, and about 0.6 at $z = 1$. The density profiles are slightly steeper in the outer regions at smaller masses. However the most prominent feature is the core radius, whose scaling departs from the self-similar behaviour $R \propto M^{1/3}$ (dotted line) below 1 keV. No significant differences are predicted in the tCDM universe. The flattening of the R – M or the R – T relation has been clearly detected in the data, and related to heating processes, by Mohr & Evrard (1997); note, however, that they plotted an isophotal radius, which is a much better defined quantity from the observational point of view. Smaller cores are found at higher z , since all the linear dimensions are reduced approximately by a factor $(1 + z)$.

We note that our results differ from those found by Fujita & Takahara (2000). In fact, their assumption of isothermality allows to relate the β parameter directly to the temperature of the external gas. This is no longer valid in our model, where the entropy of the external gas affects the dimension of the adiabatic core r_c , breaking the self-similar scaling, while yielding a β parameter independent of the mass.

Finally, we note that our values of β are somewhat larger than that observed in clusters (see Mohr, Mathiesen & Evrard 1999). This may be due to our fitting procedure, that extends up to the shock radius. In fact, our profiles are steeper than a β -model at large radii, and the best fits usually give larger β for larger cores in order to reproduce the rapid steepening of the profiles out of the core. The outer regions are generally too weak to be detected in ROSAT data, since their surface brightness is below 10^{-15} erg s $^{-1}$ cm $^{-2}$ arcmin $^{-2}$ (see TSN00). On the other hand, such a regions are expected to be efficiently detected in the future Chandra and XMM data.

4.2. The effect of Cosmology and Dark Matter

From the considerations above, it is clear that the level of the initial adiabat strongly affects the final properties of the ICM, and that, in principle, it is not necessary to invoke substantial heating after the collapse, provided that $K_{34} \simeq 0.3$. The profiles are affected also by changing the cosmological background, the epoch of observations, or the dark matter profile. To show these variations, not directly related to the entropy, in Figure 9 we plot the density and temperature profiles, along with the polytropic index, for a typical massive cluster ($0.6 \times 10^{15} h^{-1} M_\odot$, corresponding to a virial temperature of $k_B T \simeq 5$ keV) changing in turn cosmology, epoch and dark matter profile and comparing them to the case with Λ CDM at $z = 0$, NFW profile, $K_{34} = 0.4$. The cooling is included for all the cases.

A steeper dark matter profile (Moore et al. 1998) gives higher gas densities in the center (dashed line). The temperature gradient is correspondingly larger. In any case γ_p is always bounded between 0.9 and 1.2 outside the adiabatic core. In principle, observations can discriminate between different dark matter profiles, and the observed temperature profiles (see Markevitch 1998) would favour profiles steeper than NFW, but we recall that this minor effect can be overwhelmed by changes in the entropy or by the presence of substructure.

At higher redshifts (here we focus on a typical value of $z = 1$ which is the nominal goal of the future X-ray surveys) the adiabatic accretion is relatively more extended in time during the lifetime of the object, and, for the same value of K_* , the imprint of the background entropy is more evident. This is because virialized objects form at a total density contrast which is almost constant with respect to the critical density, and the baryons will consequently reach larger densities before being accreted. These larger densities translate into pre-shock temperatures larger approximately by a factor $(1 + z)^2$, and thus in a larger sound speed $c_s \propto (1 + z)$. On average, the shock condition is harder to satisfy since the infalling velocities scale only as $v_i \propto \sqrt{1 + z}$, and, consequently, a larger number of baryons are accreted adiabatically. The resulting density and temperature profiles are flatter (dot-short dashed line). This effect adds to the flattening of the total dark matter profile at high redshift, as envisaged by NFW. As we will see, this mechanism is responsible for keeping the $L-T$ relation approximately constant with redshift.

The case for a tCDM cosmology at $z = 0$ (dotted line) shows flatter profiles. This is easily understood if we recall that the external density is proportional to the mass accretion rate, and that the mass accretion rates are higher at $z = 0$ in tCDM with respect to Λ CDM (similar to the rates at $z = 1$ in Λ CDM for objects of the same mass). In general, the cosmology does not have a large effect on the evolution of the $L-T$.

4.3. The Shock Radius and the Baryonic Fraction

The boundaries of the emitting gas are given by the shock radius of the last accreted shell, where there is a discontinuity between the inner hot gas and the outer cooler gas. The outer unshocked gas gives also a contribution to the emission, and can be detected in the outskirts of rich clusters giving important information on the entropy level of the external baryons (TSN00). It always gives a small contribution if compared to the total emission from the cluster, and here it is neglected. For very small mass objects, the last accretion radius is quite distant from the virial radius, in a region of very low density and very low infall velocity. The shocks are typically very weak, and the gravitational entropy production is negligible. In such low mass objects the X-ray emission is expected to fade outwards without discontinuity.

The position of the last accreting shell is calculated simply using mass conservation. In fact, following Equation (5), the total mass of diffuse baryons involved in the cluster collapse, is equal to the mass included in the initial comoving region, $M_B = f_B M$, after subtraction of the baryons in stars and the cooled baryons in the center which depend on epoch and mass. Due to the different distribution of the baryons with respect to the dark matter, the ratio of the shock to the virial radius is a function of epoch and of the total mass accreted, as shown in Figure 3. In Figure 10(a) we show the position of the final shock radius with respect to the virial one at redshift $z_0 = 0$. At small masses, where the gas distribution is flatter and more extended, the shock radius can be approximately $\simeq 2$ times larger than the virial radius. In other words, the external gas does not fall into the potential well, but is accumulated at large radii. At very high masses the accretion rates are larger, and the pressure term can be important, giving, for high density universes, a shock radius slightly smaller than the virial radius. The same happens at higher redshift when the accretion rates are correspondingly larger. In any case, for large mass systems the shock radius is expected to remain close to the virial radius of the cluster, as was predicted in numerical simulations (see, e.g., Takizawa and Mineshige 1998). Slightly larger shock radii are predicted for higher values of the background entropy.

Here, the ratio of the mass in baryons within the shock radius to the total mass within the virial radius, is, by definition, always equal to the universal average baryonic fraction. However, since the two radii are generally different, the observed baryonic fraction within the virial radius will be a growing fraction of the mass scales. In Figure 10(b) the baryonic fraction within the virial radius R_v is shown as a function of the total virialized mass. The largest variations are between masses 10^{13} and $10^{14} h^{-1} M_\odot$, roughly corresponding to temperatures below 1 keV at $z = 0$. In any case, any entropy excess, irrespective of the origin (external or internal) always tends to puff up the baryons with respect to the dark matter (as observed in numerical simulations, see Pearce et al. 1994, Tittley & Couchman 2000). This reinforces the case for a low density universe derived from the observed high ratio of baryonic to total mass.

4.4. The Energy Budget

An important quantity is the amount of non-gravitational energy per particle corresponding to K_* . The temperature corresponding to a given adiabat is $k_B T \simeq 3.2 \times 10^{-2} K_{34} (1 + z_h)^2 \delta^{2/3}$ keV, where δ is the overdensity with respect to the ambient density at z_h , and z_h is the epoch of the heating. The assumption of an initial and homogeneous K_* , implies that the entropy of each shell must be in place at turn-around. At this epoch the density of the shell is assumed to be the background value. Thus, the minimum energy released in the gas can be computed as

$$k_B T_{min} = 3.2 \times 10^{-2} K_{34} \frac{1}{M_0} \int_0^{M_0} [1 + z_{ta}(M)]^2 dM. \quad (12)$$

In the case of a Λ CDM universe we have $k_B T_{min} \simeq 0.1 (K_{34}/0.4)$ keV with a small dependence on the final mass M_0 .

As we have already discussed, starting from a high adiabat is not the only way to prevent massive cooling, since non-gravitational heating in the center of the clusters could help in re-establishing the entropy floor. However, the energy needed to re-establish the entropy floor after accretion is much higher than the energy needed to put the baryons initially on the *right adiabat*. If the baryons are heated preferentially at higher density the excess energy is higher by a factor $\delta^{2/3}$. However, this is not the only reason for a larger energetic budget. In fact, another advantage in heating the gas at lower densities, is that radiative cooling is not able to re-emit the energy on very short time-scales.

To make a simple example without the cooling, if the baryons are heated at $z \simeq 0$ when they are at an average density contrast equal to 200, typical of virialization, we would obtain $k_B T \simeq 0.3$ keV. However, this value underestimates the real energy budget, since the density in the center, where the entropy excess is expected, is much higher than the average contrast, and $z \simeq 0$ is in any case too late to inject the extra energy. A more realistic calculation for the center of rich clusters can require more than 2 keV per particle (see §7 and TSN00) to establish a density core and eventually halt the cooling in the center. This arguments show clearly how the same entropy level, which determines all the X-ray emission properties, can be due to very different heating balances. In this respect, the distribution of metallicity in the ICM may be useful in calculating the actual amount of excess energy dumped into the baryons.

4.5. The Luminosity–Temperature–Mass relations and the Entropy–Temperature plot

We can derive the average relation between the bolometric luminosity, the emission weighted temperature and the total virialized mass. The bolometric luminosity over the whole emitting volume defined by R_s is:

$$L_x = \int_0^{R_s} \epsilon(r) dV \text{ erg s}^{-1}, \quad (13)$$

where $\epsilon(r)$ is the emissivity per unit volume, including free-free and line emission, expressed by:

$$\epsilon = n_e n_i \Lambda_N \text{ erg s}^{-1} \text{ cm}^{-3} \quad (14)$$

where n_e and n_i are the electron and ion density respectively, and Λ_N is the normalized cooling function depending on temperature and metallicity (from Sutherland & Dopita 1993). We adopt a value of $Z = 0.3 Z_\odot$, as observed on the scale of clusters ($k_B T > 2$ keV). Such a value is currently observed on the scale of groups with large uncertainties, due to difficult line diagnostic and poor temperature resolution (Renzini 1997; Buote 2000). However, since the cooling function includes emission over a range of energies wider than the usual X-ray bands, we cut the emission at energies lower than 0.1 keV.

The emission weighted temperature defined over the entire emitting volume is:

$$k_B T_{ew} \equiv \frac{\int_0^{R_s} k_B T(r) \epsilon(r) dV}{\int_0^{R_s} \epsilon(r) dV} \text{ keV.} \quad (15)$$

The results are shown in the Figures 11 and 12 for Λ CDM and tCDM respectively for $K_{34} = 0.3$, with the inclusion of cooling. The self-similar case is shown for comparison (dashed line). Data are taken from Arnaud & Evrard (1999) and Allen & Fabian (1998) for the clusters, and from Ponman et al. (1996) for the groups. An important issue here is that the total luminosity emitted by all the accreted gas (light curves in Figures 11 and 12), overestimates the luminosities found by Ponman et al. (1996) at temperatures below 1 keV. This is because the luminosities of the observed groups are defined within the fixed projected radius of $100h^{-1}$ kpc. Therefore we also calculated the luminosity and the emission weighted temperature performing the integrals of Equations (13) and (15) over the cylindrical volume defined by the projected radius of $100h^{-1}$ kpc. We show both the total luminosity, including all the gas even at $R_s \gg R_v$, and the luminosity within $100h^{-1}$ kpc. The lower values with respect to the global $L-T$ relation is due to a factor of $\simeq 1/3$ in luminosity due to the exclusion of the low surface-brightness gas at radii larger than $100h^{-1}$ kpc, and by the factor of ≤ 2 gained in the emission weighted temperature since only the inner regions, with strong temperature gradients, are included. Thus, in the simple scenario of an external K_* , the groups are expected to be surrounded by a large halo of surface-brightness $\simeq 10^{-16}$ erg s $^{-1}$ cm $^{-2}$ arcmin $^{-2}$. Its detection would constitute an important test for the external entropy scenario (TSN00).

In Figure 11 we also show the prediction for the luminosity within $100h^{-1}$ kpc in the cases $K_{34} = 0.2$, which turns out to give better fits for the groups. Thus, even if clusters with $k_B T > 2$ keV seems to require $K_{34} \simeq 0.3 - 0.4$, a lower value $K_* \simeq 0.2$ gives a better fit to the low end of the $L-T$ relation. As we will see, this is confirmed by the entropy-temperature relation (see Figure 17).

It is clear how the presence of the background entropy bends the $L-T$ relation from the self-similar slope to an average $L \propto T^3$. However, with this simple model it is difficult to reproduce the steepening below 1 keV. This is partially due to inclusion of line emission, that prevents the

L – T relation from reaching the adiabatic slope $L \propto T^5$. In fact, for a metallicity $Z > 0.1Z_{\odot}$ the slope of the emission curve between 0.3 – 1 keV is virtually zero, or even negative. In this case the asymptotic slope will be flatter than T^4 .

The M – T relation at small masses is lower with respect to the relation between mass and virial temperature (dashed lines, see Equation (2.2) in Eke et al. 1998) which is reproduced by our self-similar case. The predicted M – T relation in Λ CDM with $K_{34} = 0.4 \pm 0.2$ is consistent with the recent finding of Nevalainen, Markevitch & Forman (2000). Note that the values plotted in Figures 13 and 14 are re-scaled to the virial mass from the mass quoted in the paper, using the corresponding NFW profile. The steepening of the temperature profiles in the adiabatic cores gives higher emission weighted temperatures, about $\simeq 25\%$ larger than the corresponding virial temperatures for $k_B T < 2$ keV. This translates into an uncertainty of less than a factor of 2 in the total mass (using the self-similar relation). The evolution is similar to that of the self-similar case, and the difference in slope is preserved. In the tCDM case, the M – T relation is higher and gives a poor fit to the data of Nevalainen, Markevitch & Forman (2000).

The slope of the L – T relation is affected by different values of K_* as shown in Figure 15 at $z = 0$ in a Λ CDM universe. Lower values gradually approach the self-similar relation $L \propto T^2$. However, the self-similar scaling is never reached in the limit $K_* \rightarrow 0$, due to the cooling catastrophe. We recall that our ability to include the cooling processes in the cases presented here, is due to the non-negligible initial entropy level. If $K_{34} \ll 0.05$, the cooling processes are too strong and our computation scheme becomes inadequate. The M – T relation is less affected by changes in K_* (see Figure 16).

All the above physics influences the relation between the central entropy (measured at a radius $r = 0.1R_v$) and the temperature, as shown in PCN. The emergence of the entropy floor at small scales (low temperatures) is directly seen as a departure from the self-similar expectations, shown as a dashed line in Figure 17². Note that in this case the adiabat is defined differently, using the electron density instead of the mass density: $K_P \equiv k_B T / n_e^{2/3}$ keV cm². The relation between the two definitions is $K_P = 0.95 \times 10^3 K_{34}$. In this respect, the value observed should be considered indicative of the average entropy in the center of the halos. The entropy floor is clearly matched at $k_B T < 2$ for $0.1 < K_{34} < 0.4$. In particular, $K_{34} = 0.2 – 0.3$ reproduce both the L – T and K – T relations over the whole temperature range.

²The entropy is computed using the predicted local value of the temperature at $r = 0.1R_v$; very similar values are obtained using the emission weighted temperature as effectively used in PCN

5. THE ENTROPY HISTORY OF THE UNIVERSE AND THE X-RAY EVOLUTION OF CLUSTERS

From the above results, it is clear that a significant background entropy, S_* , present in the IGM before the formation of large dark matter halos affects the X-ray properties of groups and clusters and can explain many scaling properties. However, the assumption of a uniform floor of entropy for all the baryons could be too simplistic. As we showed, the data seems to require a growing value of K_* at larger mass scales: $K_{34} \simeq 0.2$ for $k_B T < 2$ keV, and $K_{34} \simeq 0.4$ for $k_B T > 2$ keV. In terms of physical mechanisms, it is reasonable to expect that S_* is correlated with higher density regions where star formation or nuclear activity preferentially occurs. For example, if the excess entropy is linked to star formation processes, an entropy excess should be observed in the diffuse baryons expelled by galaxies at high redshift. The distribution of entropy should follow the light distribution, and should show a dependence on cosmic time that parallels the birth of the first stars and QSOs. This topic can be addressed not only with X-ray observations, but also with the UV and optical investigation of the low density baryons detected, e.g., as Ly α clouds. Here we will discuss in greater detail the scenario with a uniform external entropy, but relaxing the assumption of a constant K_* .

We already know that the IGM which is observed in high- z Ly α clouds generally shows an entropy level lower than that observed in the centers of groups. An approximate relation derived from the observations is $K_{Ly\alpha} = (1.2 \pm 0.5) 10^{-2} (1+z)^{-1} \times 10^{34}$ erg g $^{-5/3}$ cm 2 (extrapolated from Figure 10(b) in Ricotti et al. 2000, see also Schaye et al. 1999). Thus, the ratio of the value K_{gr} observed in the center of the groups to that observed in Ly α is about $K_{gr}/K_{Ly\alpha} \geq 10(1+z)$. This may indicate that the ICM baryons undergo substantial heating with respect to the baryons observed in Ly α or, possibly, that the baryons seen in Ly α clouds are not the same baryons that will be later accreted in clusters. Furthermore, the chemical properties of the IGM seen in the Ly α forest are clearly different from those of the ICM in clusters, showing that the ICM was affected by star formation processes and chemical enrichment to a larger extent with respect to the Ly α clouds, with a commensurate amount of entropy production. In this respect, it will be interesting to observe the tenuous gas being accreted in the outskirts of nearby, large clusters, but not yet shocked, or at large radii in small groups, and compare it with the gas observed in different environments at different cosmic epochs. Such observations would complement the investigation of the entropy excess as observed in nearby and distant clusters.

As expected, the evolution of the background entropy affects both the evolution and the shape of the $L-T$ relation. We already emphasized the fact that the uncertainty in the evolution of the $L-T-M$ relations reflects on the uncertainty in the derivation of cosmological parameters from the cluster abundance evolution. The $L-M$ relation is, in fact, the link between the cluster mass function (predictable for a given cosmology with numerical or analytical calculation) and the observed X-ray luminosity distribution. The complexities due to the evolution in the luminosity are only partially avoided when directly using the temperature. In fact, selection effects for flux limited samples add to the evolution of the emission weighted temperatures (see Eke et al. 1998).

If the minimum background entropy S_* is kept constant at every epoch, the evolution of the L – T relation is essentially frozen, or mildly negative, even at redshifts as high as $z = 1$, as already shown in Figures 11 and 12. The evolution of L at fixed T_{ew} is negative especially at small temperature. This global behaviour is in agreement with the claim for null evolution of the L – T at redshift $z \simeq 0.4$ (Mushotzky & Scharf 1997). A non evolving L – T relation, suggested also by the present data on the luminosity function at high redshifts ($z > 0.5$), would strengthen a low density, eventually flat, universe (c.f. Borgani et al. 1999).

We can investigate how the evolution of the L – T is affected if the background entropy evolves substantially with epoch. In the Figure 18 and 19 we assumed $K_{34}(z) = 0.8(1+z)^{-1}$, which is an evolution that parallels the one observed in the Ly α clouds. In this scenario, objects observed at redshift $z = 1$ have accreted most of their baryonic mass when the entropy was lower, and thus mostly in the shock regime. This allows the cooling to start earlier, and be more efficient. As a net result, the L – T and the K – T relations at $z = 1$ are higher with respect to the predictions of the constant K_* scenario. However the positive evolution is about a factor of two, much less than the intrinsic scatter, and very difficult to observe. Such a positive evolution is too small to reconcile a critical universe with the observed high redshift luminosity function. As a further comment, we recall that the large discrepancy between the average level of entropy seen in Ly α clouds and that observed in the center of groups, implies that the Ly α gas is not the same or the heating rate is much steeper than this. We therefore adopt this entropy evolution as a reference case.

Assuming $K_{34} = 0.8(1+z)^{-1}$, gives a good fit to the whole temperature range without requiring further dependence on the mass scale. This is because the evolution $(1+z)^{-1}$ introduces by itself such a dependence. The core of intermediate mass halos are assembled at $z \simeq 1$, for an effective $K_{34}(z = 1) = 0.4$, while low mass objects build their cores at redshifts $z \simeq 2 - 3$, for $K_{34}(z = 3) = 0.2$. Also an evolution as strong as $K_{34} = 3(1+z)^{-2}$ provides a good fit to the data.

6. DISCUSSION

The main limitation of this model is clearly the adopted spherical symmetry and also the assumptions of isotropic and continuous infall. In the real world, some of the baryons are accreted in the form of smaller clumps and substructure, and flow along sheets and filaments. The spherical infall model used here does not include the effects of larger and smaller scale perturbations. Moreover, there are missing ingredients in the physics of baryons. We shall briefly discuss them in turn.

The presence of large-scale structure is not expected to affect strongly the accretion rates and in general the statistical properties of dark matter halos. In fact, the rates used in this work are derived from the PS formalism, which proves accurate within few percent when compared to N–body simulations that include large-scale structure (see, e.g., Governato et al. 1998). However, an effect of the large-scale structure which is of interest here, could be the eventual contribution to the initial

entropy in the IGM due to shocks occurring on large scales related to the formation of filaments. Hierarchical gravitational processes do not break the self-similarity, but the anisotropic collapse can produce widespread shocks that raise the average entropy level in the IGM everywhere without being associated with the formation of halos. The baryons that fall in the isotropic potential wells at the intersection of sheets and filaments could be already heated by an amount which depends on the power spectrum on large scales. This can break the self-similarity of the baryons, assuming that the large-scale heating is effective almost uniformly in the IGM.

Focusing on smaller scales, the presence of substructure in the infalling matter necessarily introduces some stochasticity in the accreting processes. The intrinsic scatter in the density and the temperature of the accreted baryons translates into a scatter in the observational quantities (see, e.g., CMT97). The presence of substructures implies some gravitational energy is transferred to the baryons before they are accreted into the main potential well and shocked for the last time. However, the gravitationally-produced entropy on small scales is very different from the above mentioned large scale production. In fact, the mass distribution of satellite halos scales self-similarly with the total mass of the final halo. Thus the amount of entropy given to the baryons in substructures scales with the final mass, and does not produce any break of self-similarity. This entropy contribution can be included in the external entropy, K_* , without any distinguishing effect with respect to the mass scale.

Another point related to the dark matter is the case of very massive merger events, where a massive, disruptive event is defined by the mass ratio of the merging halos being larger than about 0.3 (see Roettiger et al. 1998). In these cases it is likely that the ICM is strongly stirred, and, if the lookback time of the event is less than 1 Gyr, the ICM is not even in hydrodynamical equilibrium at the epoch of observation. Massive mergers can also create situations of non-equilibrium ionization (see Ettori & Fabian 1998; Takizawa 2000). It is clear that the model cannot describe the population of such disturbed clusters. In the PS formalism, the fraction of objects that are subject to large merger events is a sensitive function of both the total virial mass M_0 and the observation epoch z_0 . We calculate that the expected number of major mergers in the last Gyr is between 0.1 and 0.2 in tCDM, and a factor of 2 lower in Λ CDM, at $z_0 = 0$ (for a mass range between 10^{15} and $10^{13} h^{-1} M_\odot$). However, such numbers grow to 1–0.5 at $z_0 = 1$ in tCDM and 0.6 – 0.3 in Λ CDM. In this framework, it is reasonable to expect that at $z \simeq 1$, a fraction between 1/3 and 1/2 of the population of clusters has undergone a massive merger event with a lookback time less than 1 Gyr. This has to be regarded as an intrinsic limitation to statistical analyses of the population of high redshift clusters.

Other limitations come from the more complex physics of baryons. An important issue is that the entropy in the center may increase because shocks propagate in the inner part of the halos due to infalling gas along filaments (A. Klypin 2000, private communication). We stress however, that in order to survive the outer shock and propagate in the very central part of the halo, the infalling baryons should be compressed already. The presence of an initial entropy level will inhibit the formation of dense knots of gas at least on small scales, and thus inner shocks are probably

limited only to very massive mergers.

Another important component, which is not included in the present model, is the momentum gained from the heated gas, that can push part of the baryons out of the halos without contributing to the average heating. This effect is very difficult to model a priori. Its effect on the X-ray emission can be computed by including semianalytical models of galaxy formation (see Menci & Cavaliere 2000).

Finally, gravitational effects of the baryons on the dark matter profile are neglected. These can be important in the very center, where the baryons can concentrate in the form of cooled gas and contribute to density peaks which may affect the X-ray emission (see Pearce et al. 2000, Lewis et al. 2000).

7. CONCLUSIONS

We have presented a detailed model to relate the X-ray properties of diffuse baryons in clusters of galaxies to the entropy history of the cosmic baryons, after including adiabatic compression, shock heating and cooling. Our aim is to build a useful tool to reconstruct the entropy history of the universe from the observations of local and distant clusters. In particular, a major goal is to identify and follow in time the processes that generate the entropy excess. This entropy excess is now probed by many observations and it is connected with many scaling properties of X-ray halos. Even if a given entropy excess does not translate into a unique heating history, the comparison of X-ray data with observations in other bands may allow identification of the major heating sources. Favoured candidates are star formation processes and nuclear activity. At present, however, neither the epoch, nor the source of the related heating process have been identified.

In this paper we have limited the investigation to a scenario in which the excess entropy is present since very high z and is uniform throughout the IGM. A case with an external entropy decreasing with redshift, mimicking the rise of a population of heating sources, is also presented. In both the constant and time-evolving case, the scaling properties of local clusters of galaxies are reproduced on a large range of scales, with an appropriate choice of the free parameter K_* . The properties of distant X-ray halos are predicted to be generally similar to properties of the local population, but significative differences can be actually observed by the present-day X-ray satellites, shedding light on the thermodynamics history of the ICM. We recall here the general results on density and temperature profiles, together with the results on the evolution of the global X-ray properties, especially luminosity and emission weighted temperatures.

The bending of the $L-T$ relation with respect to the self-similar case $L \propto T^2$, is due to the flatter profiles of the ICM going from large mass to small mass halos. Good fits are obtained for a background entropy in the range $K_* = (0.2 \pm 0.1) \times 10^{34} \text{ erg cm}^2 \text{ g}^{-5/3}$ for $k_B T_{ew} < 2 \text{ keV}$, and $K_* = (0.4 \pm 0.1) \times 10^{34} \text{ erg cm}^2 \text{ g}^{-5/3}$ for $k_B T_{ew} > 2 \text{ keV}$. This scale dependence can be introduced by an evolution in the effective value of K_* . In particular, $K_{34} = 0.8(1+z)^{-1}$ gives a good fit over

the whole range of observed temperatures.

The central regions of groups and clusters, which dominate the X-ray emission, are formed during the initial stages of accretion. In these early phases, if a significant background entropy is present, the accretion is adiabatic, and the gas is compressed in a flat, low density profile with steep temperature gradients. This is relevant for the smallest halos, where the gravity does not overcome the pressure support of the baryons for the majority of the subsequent accretion of gas. In clusters the infall velocities rapidly become larger than the sound speed, and the shock regime takes over. In the outer regions of clusters the entropy is entirely due to gravitational processes, and the entropy profile is a featureless power law approaching $K \propto r^{1.1}$.

This mechanism is particularly efficient if cooling is neglected. However, it is known that the cooling is an important ingredient in the history of the ICM. The main effect is that the isentropic cores expected in the constant entropy scenario, are partially erased by the process of cooling. Still, if $K_* > 0.1 \times 10^{34} \text{ erg cm}^2 \text{ g}^{-5/3}$, the cooling processes are significantly suppressed and the inner regions of the halos keep the imprint of the initial entropy level. Cooling processes appear again only in massive halos, where the gravity dominates the energy of the system and the excess entropy is no longer able to keep the gas at low density. In the extreme case of negligible K_* , it is worth noting that the cooling processes alone would have a dramatic effect on both small and large mass halos. In small mass halos ($10^{13} M_\odot$) most of the gas is expected to cool and recombine, causing a central *baryonic catastrophe*.

Other important characteristics are found in the temperature structure especially of smaller halos. Temperature gradients are commonly expected both in clusters and in groups. The polytropic index is predicted to be $\gamma_p \simeq 0.9 - 1.2$ in the region where the gas is shock heated. The polytropic index can be higher if the dark matter profile is centrally peaked (e.g., with a power law with index ~ -1.4 , see Moore et al. 1998). Another relevant observable (for local halos) is the position of the final shock radius, which is expected to be close to the virial one at large mass scale, while it migrates to larger radii in small groups. In the smallest halos, in fact, the shock is vanishingly small. As a function of epoch, for a given object, the shock/accretion radius is initially quite distant from the virial radius. It is very close to the virial radius when the mass accretion rate reaches its maximum and the shock regime is well developed. Eventually, the mass accretion rate decreases (especially in the Λ CDM universe) and the shock radius relaxes again to larger positions. A consequence of the above picture is that the ratio of the baryonic mass included in the virial radius to the total mass, is always lower but still close to unity; it can be significantly lower (1/3) only for small mass halos (corresponding to emission-weighted temperatures of 0.3 – 1 keV).

It is remarkable that the simple presence of an initial excess entropy in the diffuse IGM can reproduce many of the scaling properties of the observed X-ray halos, without the contribution of any internal heating. It is interesting to discuss the implications of this simple scenario for the energetic budget and the past cosmic star formation history. The minimum excess energy associated

with an initial background entropy K_{34} is about

$$k_B T \simeq 0.1 \left(\frac{K_{34}}{0.4} \right) \text{ keV}, \quad (16)$$

where the gas is assumed to be at the background density at the epoch of the heating. However, we can speculate on the energy budget when the entropy excess is generated after the collapse, at much larger densities (the internal scenario).

Following PCN, we can establish a relation between the epoch of heating and the energy released. Under the assumption that the heating process can be described with a single epoch and a typical overdensity, we have:

$$1 + z_h = \left(\frac{k_B T_h}{3.2 \times 10^{-2} K_{34}} \right)^{1/2} \delta^{-1/3}, \quad (17)$$

where $k_B T_h$ is the average energy per particle released in the IGM by non-gravitational processes. If we adopt the conservative scenario in which the gas is heated at a typical virial density ($\delta \simeq 200$), to have an entropy level in the range $K_* = (0.4 \pm 0.2) \times 10^{34} \text{ erg cm}^2 \text{ g}^{-5/3}$, we obtain:

$$1 + z_h \simeq (1.5 \pm 0.3) \left(\frac{k_B T_h}{1 \text{ keV}} \right)^{1/2}. \quad (18)$$

Thus, if we want heating at $z > 1$ in order to avoid the overcooling catastrophe, the energy budget must be larger than 1 keV per particle. The above estimate would give even larger values after the inclusion of cooling. In fact, if the gas is heated at high densities, most of the extra energy is likely to be re-emitted soon, and this would raise the energetic budget for a given final entropy excess. In this respect, the relation between the epoch of heating and the energy released is strongly dependent on the physical process. Of course, a scenario in which the extra entropy is provided by the contributions of several different sources, active at different epochs, is a likely possibility. In this perspective, the measure of metallicities as a function of the entropy of the baryons in different systems, from Ly α clouds to rich clusters, may be useful in determining whether the excess entropy is linked to star formation processes.

The assumption of an initial excess entropy uniformly diffused in the IGM, offers new perspectives in the approach to cluster formation, but also galaxy formation. Such an entropy background, once established, may affect the star formation itself, since the cooling processes on all scales are virtually inhibited. This is the mechanism which is expected to solve the *cooling catastrophe* (see White & Rees 1978, Blanchard, Valls Gabaud & Mamon 1992; Prunet & Blanchard 1999) and in this view X-ray clusters and galaxy formation processes are intimately related. Current attempts to model *ab initio* the physics of the heating process, and then link the entropy history of the cosmic baryons to galaxy formation, must include the well known plethora of ingredients that has been already mentioned several times: feedback from star formation processes and SNe explosions, radiative and mechanical heating from active galactic nuclei, radiative heating from hard X-ray background, gravitational heating on large scale filaments (see Menci & Cavaliere 2000; Valageas & Silk 2000; Wu, Fabian & Nulsen 2000; Madau & Efstathiou 1999; Cen & Ostriker 1999). Such

different scenarios allow for different entropy histories of the universe, determining both the spatial distribution and the evolution of the entropy in the diffuse gas.

A promising strategy for the near future is to look directly for the distribution of the entropy in the ICM (TSN00). A direct consequence of assuming a uniform entropy everywhere in the gas, is that the groups are expected to be surrounded by large halos of low surface brightness gas, spread out over radii much larger than the virial radius of dark matter halos. This low-density gas may have been missed by observations with the ROSAT satellite, but can be detected by the XMM satellite. Its emission can enhance the total luminosity of the groups by more than a factor of 3, including the lowest energy bins of $\simeq 0.1$ keV. Another promising observational channel is the absorption from metals in the gas seen against bright X or UV sources. If the source of the background entropy is star formation, significant pollution by metals is expected.

The model presented here is to be considered a useful tool to interpret the observations of high redshift clusters, that will be provided especially by the Chandra and XMM satellites. Our aim is to build a solid link between the thermodynamics of the diffuse cosmic baryons and the emitting properties of X-ray halos, in order to be able to reconstruct *the entropy history of the universe, at high and low redshifts, from spectral and imaging X-ray observations*. This will help in understanding the source of the entropy excess and the time evolution of the corresponding heating process.

We acknowledge discussions with S. Borgani, N. Menci, and P. Rosati. We thank T.J. Ponman for discussions and for providing the data in Figure 17. We thank R. Giacconi for discussions and continuous encouragement. We thank the referee, Greg Bryan, for detailed comments. PT thanks ESO Garching for hospitality during the completion of this work. This work has been supported by NASA grant NAG 8-1133.

A. The infall velocity

We find upper and lower limits for the infall velocity of the accreted baryonic shells computed with Equation (3). The last two terms of Equation (3) depend on the densities of the shell at accretion (ρ_e) and at turnaround (ρ_{ta}). The values of the two densities are derived requiring conservation of mass, and assuming that baryons and dark matter are still not decoupled at turnaround. In particular, the exact value of ρ_e depends on the validity of the Equation (5), which is based on the assumption that the total baryonic mass accreted at every epoch is $f_B M_v$, where f_B is the universal baryonic fraction. Such an assumption can be tested with numerical simulations, and will not be discussed here.

We focus on the numerical uncertainty in the estimate of the term ΔW . The total work per unit baryonic mass done by the gravitational potential on the baryonic shell is:

$$W \equiv \int_{R_{ta}}^{R_s} \frac{GM(< r)}{r^2} dr, \quad (A1)$$

where the integral is computed along the trajectory $r(t)$. If the total mass within the shell were constant, the solution would be simply:

$$W = \frac{v_{ff}^2}{2} \equiv \left(\frac{GM_{ta}}{R_S} - \frac{GM_{ta}}{R_{ta}} \right), \quad (\text{A2})$$

where M_{ta} is the total mass initially contained in the turn-around radius R_{ta} . The free fall velocity v_{ff} refers to a test particle falling from turnaround to the shock radius, experiencing a gravitational force always from the same amount of matter. However, the actual mass enclosed by a given baryonic shell will depend on time. We can write:

$$M(< r) = [f_B + (1 - f_B)Y(t)]M_{ta}, \quad (\text{A3})$$

since the baryonic mass inside the shell is constant, but the amount of dark matter can change by a time dependent factor $Y(t)$. The complete solution can now be formally written as:

$$W = \frac{v_{ff}^2}{2} + \Delta W = \frac{v_{ff}^2}{2} - \frac{GM_{ta}}{r_{ta}} \int_{R_{ta}}^{R_s} \frac{(f_B + (1 - f_B)Y(t) - 1)}{r^2} dr. \quad (\text{A4})$$

At this point we note that the amount of mass that is included in a given baryonic shell along its trajectory is always larger than the initial mass M_{ta} , since the collisionless shells of dark matter fall faster than the baryonic shells, which, instead, are pressure supported. Here, we neglect the shell crossing and the detailed behaviour in time, but we recall that we want the solution only at the accretion radius, which usually occurs just inside the most external caustic of the dark matter (see the self-similar model of Bertschinger 1985). Thus, we can safely assume that the total mass can only grow inside the baryonic shell. The mass excess $\Delta M/M_{ta} = (f_B + (1 - f_B)Y(t) - 1)$ can be described with a generic power law dependence on the actual position $r(t)$ of the kind:

$$f_B + (1 - f_B)Y(t) - 1 = \left(f_B + (1 - f_B)Y_s - 1 \right) \left[\left(1 - \left(\frac{r(t)}{r_{ta}} \right)^\alpha \right) \left[1 - \left(\frac{r_s}{r_{ta}} \right)^\alpha \right]^{-1} \right] \quad (\text{A5})$$

where $\alpha > 0$, and Y_s is the value at the accretion. To calculate Y_s we must know the dark matter density profile at radii larger than the virial radius. We do not propose a specific model here, instead we simply use the density profile as computed in Bertschinger (1985) as a reasonable approximation at radii larger than the virial one. We can substitute Equation (A5) in Equation (A4) and integrate, obtaining an estimate of W as a function of α . To eliminate the dependence on α , we take the limit for small and large values of α , to obtain the upper and lower values for ΔW :

$$\Delta W = [f_B + (1 - f_B)(Y_s - 1)] \frac{GM_{ta}}{r_{ta}} \left(\left[\frac{1 - x_s}{x_s} + \frac{\ln(x_s) + 1 - x_s}{\ln(x_s)x_s} \right] \pm \left[\frac{1 - x_s}{x_s} - \frac{\ln(x_s) + 1 - x_s}{\ln(x_s)x_s} \right] \right). \quad (\text{A6})$$

The last term in Equation (A6) bounds the possible values for ΔW , assuming a monotonic increase of the total mass enclosed by the infalling shell. The upper and lower values turn out to be between 10 % and 30 % during the mass history of a given halo, and are plotted in Figure 1 as dotted lines. This reflects our error in computing the infall velocities of the baryonic shells. The uncertainty in the infall velocities does not strongly affect the mass scale at which the adiabatic/shock transition occurs, since the dependence of v_i on the accreted mass is very steep when shocks begin to appear. This effect is related to the fast migration of the accretion radius from $\simeq 2R_v$ to $\simeq R_v$ (see Figure 3).

B. Cooling processes

Here we discuss how to compute the effect of the radiative cooling on each baryonic shell. The treatment of the cooling is complex and constitutes the largest uncertainty in modelling the X-ray emission from clusters in present-day numerical simulations, since the predicted luminosity of the central region can heavily depend on the adopted resolution (see, e.g., Sugino & Ostriker 1998).

There is of course no difficulty in solving Equation (8) as long as $\tau_{cool} > \Delta t$ where Δt is the time resolution. However, the time resolution needed increases dramatically when the density increases and $\tau_{cool} \sim \Delta t$, since the cooling is a runaway process. Since our calculation is based on a sequence of hydrostatic equilibria, and we do not want to end up with an heavy computation effort, we propose to use a reasonable time step (of the order of few tenths of Gyr) and solve *analytically* the energy Equation (8) for each shell within each time step. To do this we first assume that the cooling proceeds isobarically within Δt , and compute the new value of the pressure after each step to take into account the new equilibrium positions of each shell.

If the pressure is constant for each shell within Δt , the density can be expressed as a function of the adiabat K only, to give:

$$\rho = p^{1/\gamma} k^{-1/\gamma}, \quad (B1)$$

where $\gamma = 5/3$ and the variables are assumed to be normalized to the shock values as usual. The temperature is then:

$$t = k^{1/\gamma} p^{(\gamma-1)/\gamma}. \quad (B2)$$

Following Sutherland & Dopita (1993), we define the normalized cooling function $\Lambda_N \equiv \Lambda_{net} n_e n_i$, where n_e is the electron number density and n_i is the ion number density. For an average metallicity $Z = 0.3 Z_\odot$ we can approximate $n_e n_i = 0.704(\rho_B/m_p)^2$. The cooling time now can be expressed as a function of the adiabat K and the normalized cooling function Λ_N :

$$\tau_{cool} \simeq 2.13 \frac{k T_{s0} m_p}{\mu \rho_{s0}} k^{2/\gamma} p^{(\gamma-2)/\gamma} \Lambda_N^{-1}, \quad (B3)$$

where the subscripts “ $s0$ ” refer to the value at the shock. To write an analytic expression, we approximate Λ_N with a polynomial form:

$$\Lambda_N = C_1 (kT)^\alpha + C_2 (kT)^\beta + C_3, \quad (B4)$$

where the exponents take the values $\alpha = -1.7$ and $\beta = 0.5$. The constants depend on the assumed metallicity, and are chosen as in Table 2 in order to reproduce the cooling function of Sutherland & Dopita (1993) within few percent in the energy range $k_B T > 0.03$ keV.

Thus, using the canonical value $\gamma = 5/3$, the cooling time can be written as:

$$\tau_{cool} = C_\tau T_{s0} \frac{k^{6/5} p^{-1/5}}{C_1 T_{s0}^\alpha k^{\frac{3}{5}\alpha} p^{\frac{2}{5}\alpha} + C_2 T_{s0}^\beta k^{\frac{3}{5}\beta} p^{\frac{2}{5}\beta} + C_3}. \quad (B5)$$

The constant C_τ factorizes out the terms that depend on the shock condition, and can be written as:

$$C_\tau = 1.62 \times 10^2 [f_B(1 - f_{cool} - f_*)h^2(z) \delta_{so} g_{s0}]^{-1} \text{Gyr/keV}, \quad (\text{B6})$$

where δ_{so} is the overdensity with respect to the critical density at redshift z , T_{s0} is the temperature at the shock and g_{s0} is the compression factor at the shock; f_{cool} and f_* are respectively the fraction of baryons cooled in the center and the fraction of baryons locked into stars.

Equation (8) can be recast in term of the adiabat K only, and the final adiabat k_f can be recovered implicitly from the solution in the finite time step Δt (expressed in Gyr):

$$\Delta t = C_\tau T_{s0} \int_{k_i}^{k_f} dk \frac{k^{1/5} p^{-1/5}}{C_1 T_{so}^\alpha k^{\frac{3}{5}\alpha} p^{\frac{2}{5}\alpha} + C_2 T_{so}^\beta k^{\frac{3}{5}\beta} p^{\frac{2}{5}\beta} + C_3} \equiv F(k_i, k_f) \quad (\text{B7})$$

In particular, the condition $F(k_i, 0) < \Delta t$ determine if a shell with initial entropy k_i cools completely within Δt . At each epoch, the region comprised within the largest shell for which $F(k_i, 0) < \Delta t$ is included in the cooled fraction f_{cool} and excluded from the diffuse, emitting phase.

C. Concentration parameters

The concentration parameters of the dark matter profiles depend on epoch and cosmology, as shown in the numerical works of Navarro et al. (1997) or analytical models (see, e.g., Lokas 2000). A general trend is that lower mass halos are more centrally concentrated than high mass halos by virtue of the higher redshift of formation. For the same reason, halos of the same virial mass, but observed at higher redshifts, are less concentrated, since the difference in the average density at the formation and at the observation is smaller with respect to low redshift halos. The mass dependence of the concentration parameter, however, can be well approximated with power laws which change slightly as a function of epoch and cosmology. In this paper we used the following approximations:

$$c = 8.5 M_{15}^{-0.086} \quad \Lambda\text{CDM}, z = 0 \quad (\text{C1})$$

$$c = 5.4 M_{15}^{-0.070} \quad \Lambda\text{CDM}, z = 1 \quad (\text{C2})$$

$$c = 5.5 M_{15}^{-0.070} \quad \text{tCDM}, z = 0 \quad (\text{C3})$$

$$c = 4.4 M_{15}^{-0.046} \quad \text{tCDM}, z = 1 \quad (\text{C4})$$

where $M_{15} \equiv M/(10^{15} h^{-1} M_\odot)$.

REFERENCES

Abadi, M.G., Bower, R.G., & Navarro, J.F. 2000, MNRAS, 314, 759
Allen, S.W., & Fabian, A.C. 1998, MNRAS, 297, 57
Arnaud, M., & Evrard, A.E. 1999, MNRAS, 305, 631
Balbi, A., et al. 2000, ApJL submitted, astro-ph/0005124
Balogh, M.L., Babul, A., & Patton, D.R. 1999, MNRAS, 307, 463
Bertschinger, E. 1985, ApJS, 58, 39
Blanchard, A., Valls-Gabaud, D., & Mamon, G.A. 1992, A&A, 264, 365
Bond, J.R., Cole, S., Efstathiou, G., & Kaiser, N. 1991, ApJ 379, 440
Bondi, H. 1952, MNRAS, 112, 195
Borgani, S., Rosati, P., Tozzi, P. & Norman, C. 1999, ApJ, 517, 40
Bower, R. G. 1991, MNRAS, 248, 332
Bower, R. G. 1997, MNRAS, 288, 355
Bryan, G.L., & Norman, M.L. 1998, ApJ, 495, 80
Buote, D.A. 2000, MNRAS, 311, 176
Burles, S., & Tytler, D. 1999a, ApJ, 499, 699
Burles, S., & Tytler, D. 1999b, ApJ, 507, 732
Cavaliere, A., & Fusco Femiano, R. 1976, A&A, 49, 137
Cavaliere A., Menci N., Tozzi P. 1997, ApJ, 484, L21 (CMT97)
Cavaliere A., Menci N., Tozzi P. 1998, ApJ, 501, 493
Cavaliere, A., Menci, N., & Tozzi, P. 1999, MNRAS, 308, 599
Cen, R., & Ostriker, J. P. 1999, ApJ, 514, 1
David, L. P., Slyz, A., Jones, C., Forman, W., Vrtilek, S. D., & Arnaud, K.A. 1993, ApJ, 412, 479
Eke, V. R., Cole, S., Frenk, C. S., & Henry, J. P. 1998, MNRAS, 298, 114
Ettori & Fabian, A.C. 1998, MNRAS, 293, L33
Ettori & Fabian, A.C. 1999, MNRAS, 305, 834
Evrard, A. E. 1990, ApJ, 363, 349
Evrard, A. E., & Henry, J. P. 1991, ApJ, 383, 95
Fabian, A. C., & Nulsen, P. E. J. 1977, MNRAS, 180, 479
Gioia, I., Henry, J P., Maccacaro, T., Morris, S. L., & Stocke, J.T. 1990, ApJL, 357, 35
Frenk, C.S., et al. 1999, ApJ, 525, 554

Fujita, Y., & Takahara, F. 2000, ApJ, 536, 523

Governato, F., Babul, A., Quinn, T., Tozzi, P., Baugh, C. M., Katz, N., Lake, G. 1999, MNRAS, 307, 949

Gunn, J. E., & Gott, J. R. 1972, ApJ, 176, 1

Henry J. P. 1997, ApJ 489, L1

Helsdon, S.F., & Ponman, T.J. 2000, MNRAS, 315, 356

Henry J. P. 2000, ApJ, 534, 565

Horner, D.J., Mushotzky, R.F., & Scharf, C.A. 1999, ApJ, 520, 78

Kaiser, N. 1986, MNRAS, 222, 323

Kaiser, N. 1991, ApJ, 383, 104

Knight, P. A., & Ponman, T. J. 1997, MNRAS, 289, 955

Lacey, C., & Cole, S. 1993, MNRAS, 262, 627

Lange, A.E., et al. 2000, submitted to Phys. Rev. D, astro-ph/0005004

Landau, L. D., Lifshitz E. M. 1959, *Fluid Mechanics* (London, Pergamon press), p. 329

Lewis, G.F., Babul, A., Katz, N., Quinn, T., Hernquist, L., & Weinberg, D. 2000, ApJ, 536, 623

Lloyd-Davies, E. J., Ponman, T. J., & Cannon, D.B. 2000, MNRAS, 315, 689

Lokas, E.L. 2000, MNRAS, 311, 423

Loewenstein, M. 2000, ApJ, 532, 17

Markevitch, M. 1998 ApJ, 504, 27

Mathews, W. G., & Bregman, J. N. 1978, ApJ, 224, 308

Madau, P., & Efstathiou, G. 1999, ApJL, 517, 9

Menci, N., & Cavalieri 2000, MNRAS, 311, 50

Metzler, C. A., & Evrard, A. E. 1994, ApJ, 437, 564

Mohr, J.J., & Evrard, A.E. 1997, ApJ, 491, 38

Mohr, J.J., Mathiesen, B., & Evrard, A.E. 1999, ApJ, 517, 627

Moore, B., Governato, F., Quinn, T., Stadel, J., & Lake, G. 1998, ApJL, 499, 5

Mushotzky, R. F., & Scharf, C. A. 1997, ApJ, 482, 13

Navarro, J.F., Frenk, C.S., & White, S.D.M. 1997, ApJ, 490, 493

Nevalainen, J., Markevitch, M., & Forman, W. 2000, ApJ, 536, 73

Pearce, F.R., Thomas, P.A., Couchman, H.M.P. 1994, MNRAS, 268, 953

Pearce, F.R., Thomas, P.A., Couchman, H.M.P., & Edge, A.C. 2000, MNRAS, 317, 1029

Pen, U. 1999, ApJL, 510, L1

Ponman, T. J., Bourner, P. D. J., Ebeling, H., & Böhringer, H. 1996, MNRAS, 283, 690

Ponman, T. J., Cannon, D. B., & Navarro, F.J. 1999, Nature, 397, 135 (PCN)

Press, W.H., & Schechter, P. 1974, ApJ, 187, 425

Prunet, S., & Blanchard, A. 1999, preprint, astro-ph/9909145

Renzini, A. 1997, ApJ, 488, 35

Renzini, A. 1999, in Chemical Evolution from Zero to High Redshift, Edited by Jeremy R. Walsh, Michael R. Rosa. Berlin: Springer-Verlag, 1999, p. 185

Ricotti, M., Gnedin, N. Y., & Shull, J. M. 2000, ApJ, 534, 41

Riess, A. G. et al. 1998, AJ, 116, 1009

Roettiger, K., Burns, J., & Loken, C. 1993, ApJ, 407, L53

Roettiger, K., Stone, J. M., Mushotzky, R. F. 1998, ApJ, 493, 62

Rosati, P., Della Ceca, R., Norman, C., Giacconi, R. 1998, ApJ 492, L21

Rosati, P., Borgani, S., Della Ceca, R., Stanford, A., Eisenhardt, P., & Lidman, C. 2000, in Large Scale Structure in the X-ray Universe, eds. Plionis, M. & Georgantopoulos, I., Atlantisciences, Paris, France, p. 13

Ryu, D., & Kang, H. 1997, MNRAS, 284, 416

Schaye, J., Theuns, T., Leonard, A., & Efstathiou, G. 1999, MNRAS, 310, 57

Schindler, S. 2000, in Clustering at High Redshift, ASP Conference Series, Vol. 200. Edited by A. Mazure, O. Le Fvre, and V. Le Brun., p. 374

Suginohara, T., & Ostriker, J.P. 1998, ApJ, 507, 16

Sutherland, R. S., & Dopita, M. A. 1993 ApJS, 88, 235

Takizawa, M., & Mineshige, S. 1998, ApJ, 499, 82

Takizawa, M. 2000, ApJ, 532, 183

Tittley, E.R., & Couchman, H.M.P. 2000, MNRAS, 315, 834

Tozzi, P., Scharf, C., & Norman, C. 2000, ApJ, 542, 106 (TSN00)

Valageas, P., & Silk, J. 2000, A&A, 350, 752

White, S.D.M., & Rees, M. 1978, MNRAS, 183, 341

White, S.D.M., Navarro, J.F., Frenk, C.S., & Evrard, A.E. 1993, Nature, 366, 429

Wu, K. K. S., Fabian, A. C., & Nulsen, P. E. J. 2000, MNRAS, 318, 889

Wu, K. K. S., Fabian, A. C., & Nulsen, P. E. J. 1999, MNRAS submitted, astro-ph/9910122

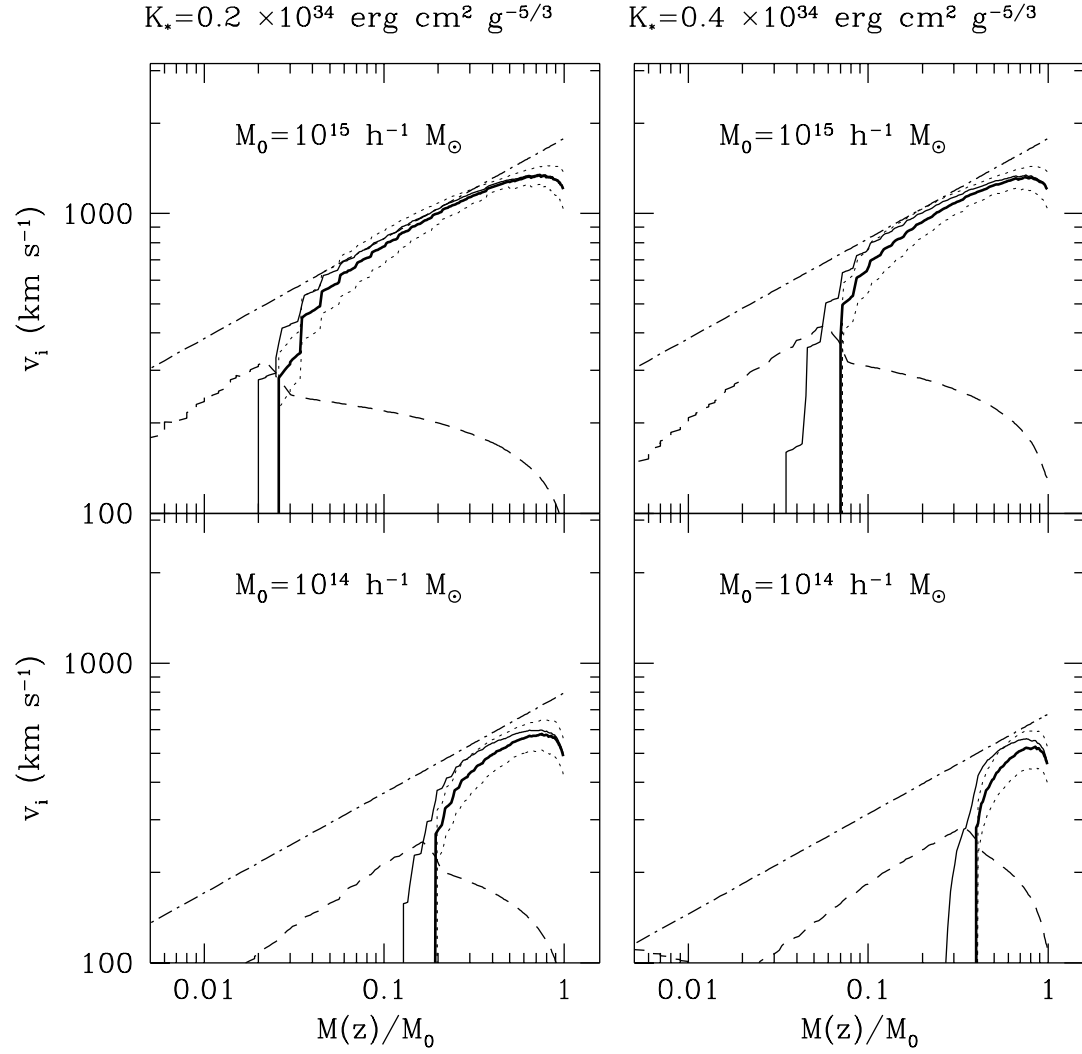


Fig. 1.— Thick solid line shows the infall velocity v_i computed at the shock radius of each baryonic shell as a function of the virialized mass (normalized to the final value). The uncertainties in v_i are shown by dotted lines. Here we assumed $K_* = 0.2$ (left panels) and $K_* = 0.4 \times 10^{34} \text{ erg cm}^2 \text{ g}^{-5/3}$ (right panels) in a low density ($\Omega_0 = 0.3$) flat cosmology (see Table 1), for a final mass at $z = 0$ of $10^{15} h^{-1} M_\odot$ and $10^{14} h^{-1} M_\odot$. The thin solid line shows the free-fall velocity at the position of the shock, while the dashed line shows the sound speed c_s computed in the gas external to the shock. When $v_i < c_s$ the accretion process is entirely adiabatic. The dot-dashed line shows the asymptotic behaviour $v \propto m^{1/3}$, which is reproduced in the strong shock regime, when the shock radius is close to the virial radius.

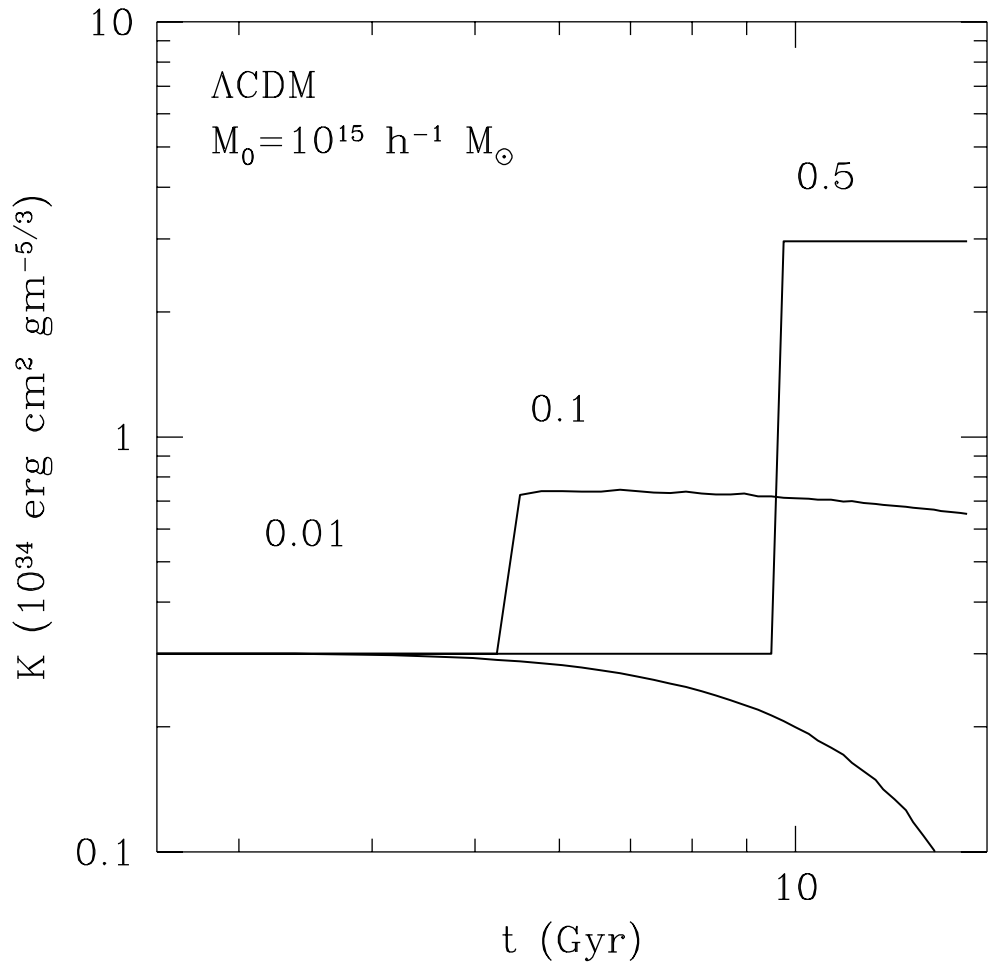


Fig. 2.— The evolution of the adiabat K for three baryonic shells is shown as a function of cosmic epoch t (ΛCDM cosmology, for a final mass of $10^{15} h^{-1} M_\odot$, $K_* = 0.3 \times 10^{34} \text{ erg cm}^2 \text{ g}^{-5/3}$). The inner shells contain 1% of the total baryons, the second 10% and the third 50%. The sharp discontinuity, increasing for outer shells, occurs at the shock.

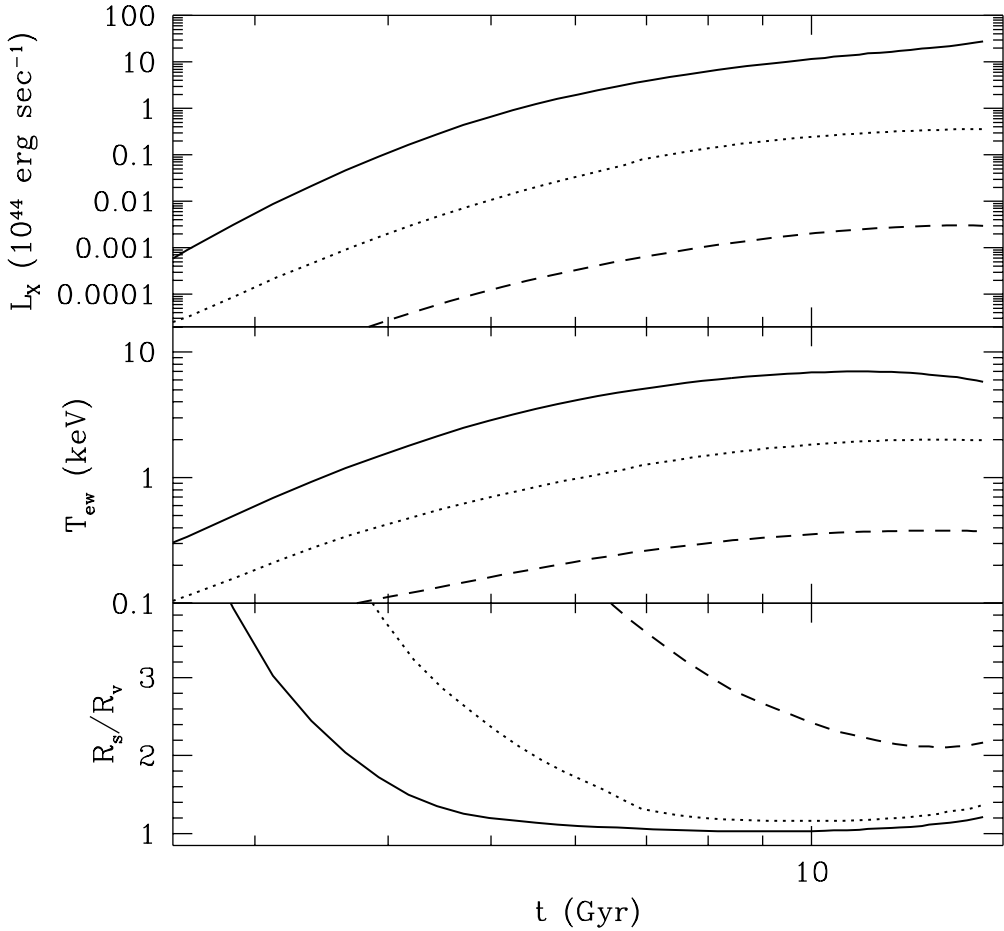


Fig. 3.— The evolution of the total bolometric luminosity L_X and of the emission weighted temperature T_{ew} is shown as a function of cosmic epoch for a final mass of $10^{15} h^{-1} M_\odot$ (solid lines), $10^{14} h^{-1} M_\odot$ (dotted lines) and $10^{13} h^{-1} M_\odot$ (dashed lines) for a Λ CDM cosmology, with a constant initial adiabat $K_* = 0.3 \times 10^{34} \text{ erg cm}^2 \text{ g}^{-5/3}$. In the third panel the evolution of the shock radius R_s , normalized to the virial radius at each epoch, is shown for the same halos.

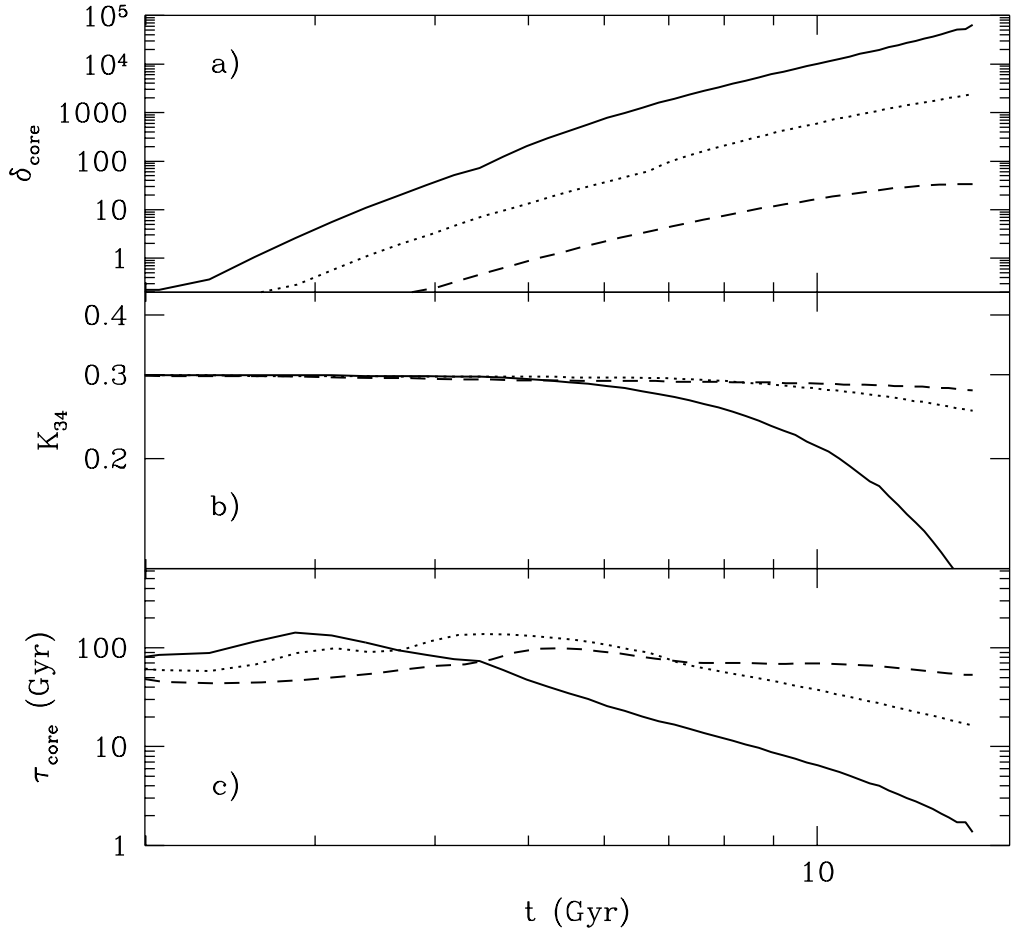


Fig. 4.— The evolution of the properties of the central adiabatic cores is shown as a function of cosmic epoch for a final mass of $10^{15} h^{-1} M_{\odot}$ (solid lines), $10^{14} h^{-1} M_{\odot}$ (dotted lines) and $10^{13} h^{-1} M_{\odot}$ (dashed lines) for a Λ CDM cosmology, with a constant initial adiabat $K_* = 0.3 \times 10^{34} \text{ erg cm}^2 \text{ g}^{-5/3}$. Panel a): average overdensity with respect to the critical value; b) average K ; c) average cooling time.

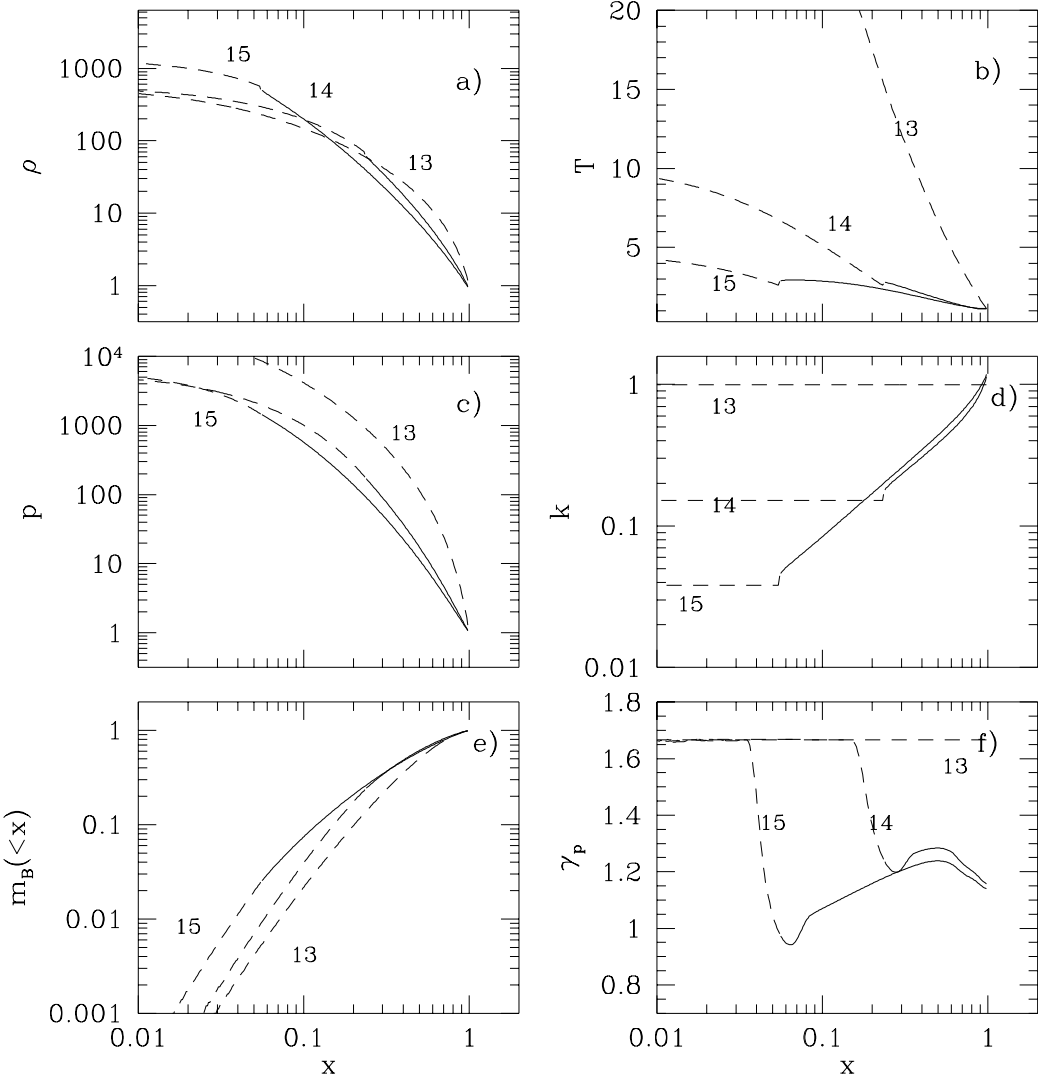


Fig. 5.— Profiles of density, temperature, pressure, entropy, baryonic mass and polytropic index as a function of the normalized radius $x \equiv R/R_s$ for clusters of different mass ($10^{15}, 10^{14}, 10^{13} h^{-1} M_\odot$ as labeled by the log of the mass) in Λ CDM at $z = 0$. Each quantity is normalized with respect to the corresponding value at the shock, in order to show departures from self-similarity. The external, initial adiabat is $K_* = 0.3 \times 10^{34} \text{ erg cm}^2 \text{ g}^{-5/3}$ constant with mass scale and epoch. The dark matter profiles are from Navarro, Frenk & White (1997). No cooling is assumed. The dashed lines are for baryons accreted adiabatically ($K(x) = K_*$), while the solid lines are for the shocked gas.

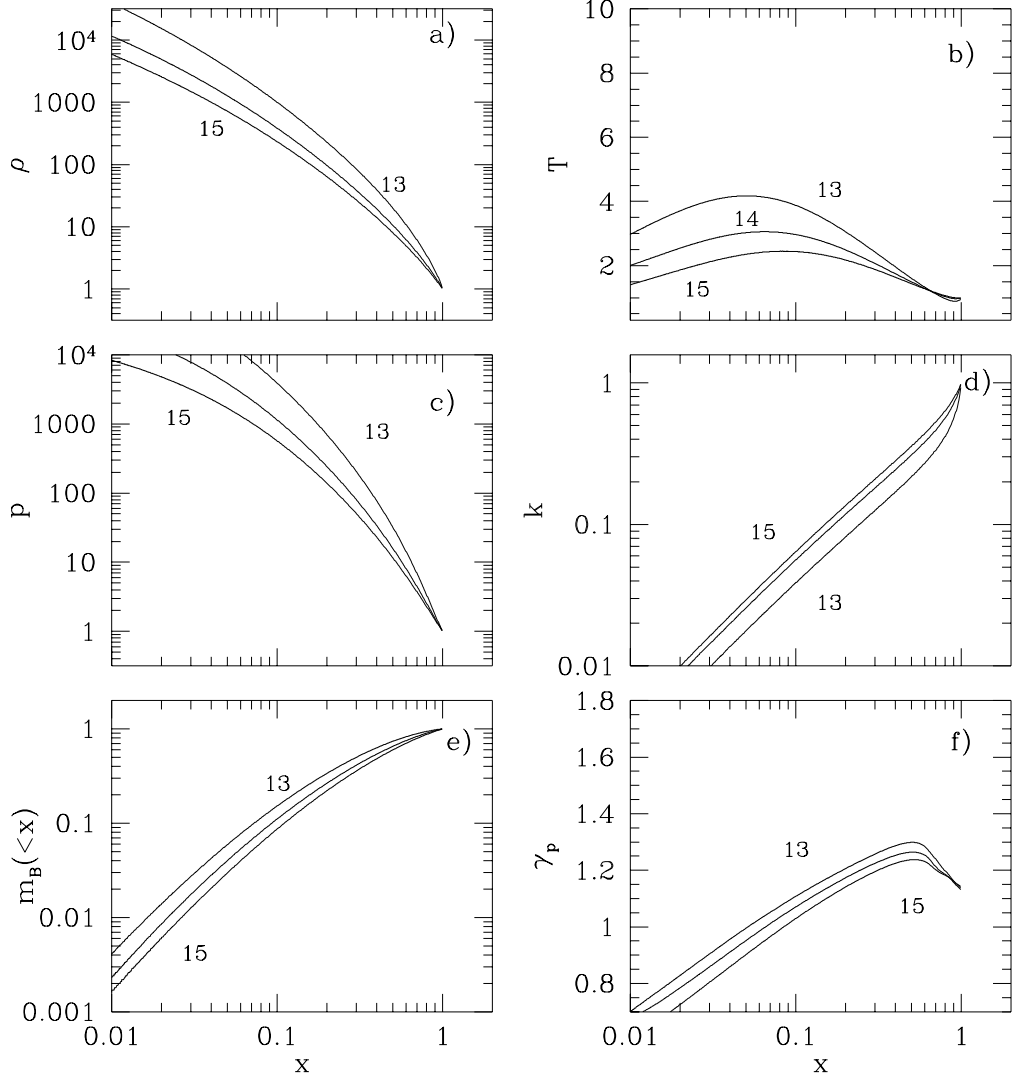


Fig. 6.— The same as in Figure 5 for Λ CDM, but with a negligible entropy and without the inclusion of cooling (self-similar case). All the gas is shocked. These profiles should be compared with Figure 5, to point out how the negligible entropy excess makes the baryons follow the dark matter and produce an opposite behaviour for which the groups are more centrally concentrated than clusters, as predicted by NFW. Note that the entropy profiles are the same at all scales.

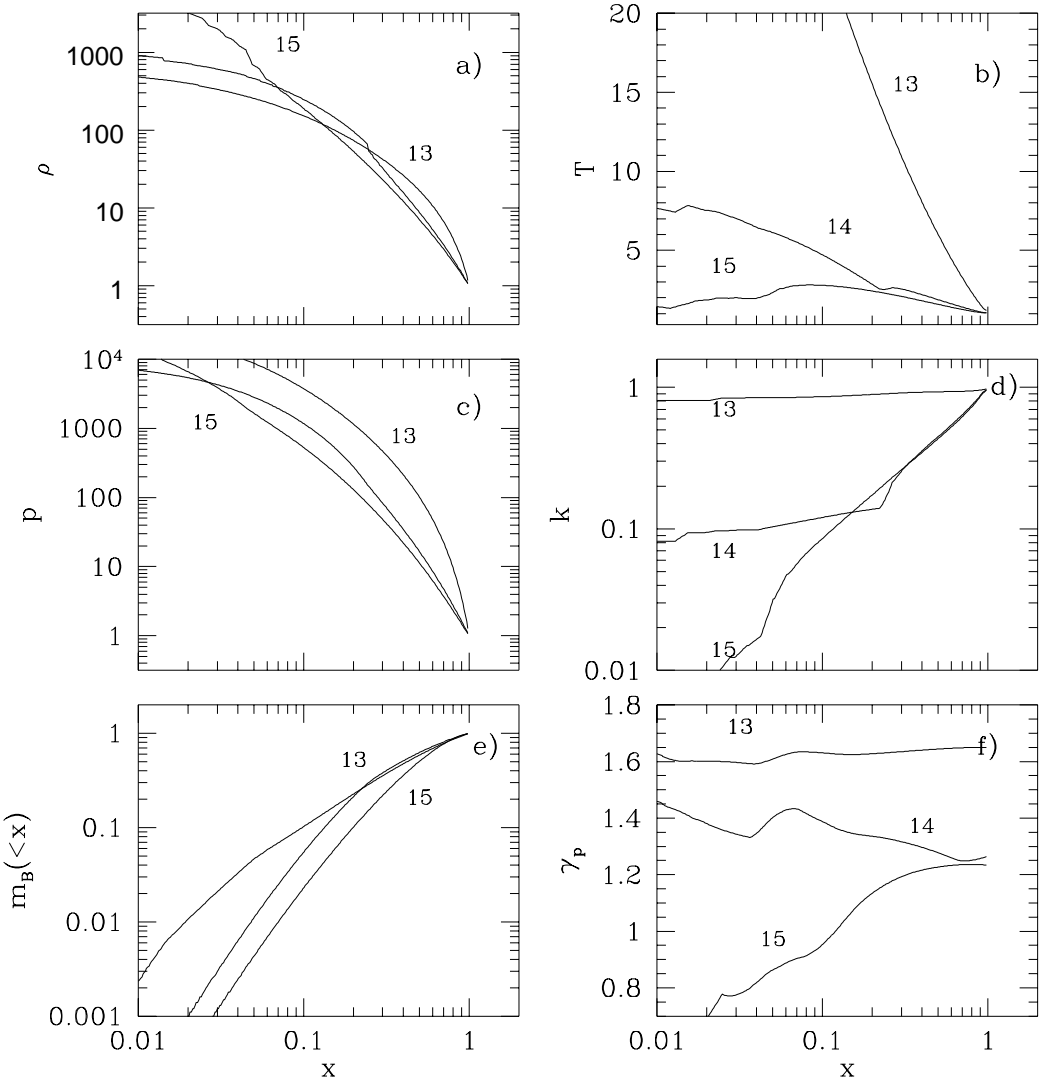


Fig. 7.— The same as in Figure 5 for Λ CDM, but with the inclusion of cooling; the external, initial adiabat is $K_* = 0.3 \times 10^{34}$ erg cm 2 g $^{-5/3}$. Note in panel d) that the entropy plateau in the center has been partially erased by cooling. The polytropic indexes γ_p are averaged over $\Delta \log(x) = 0.3$.

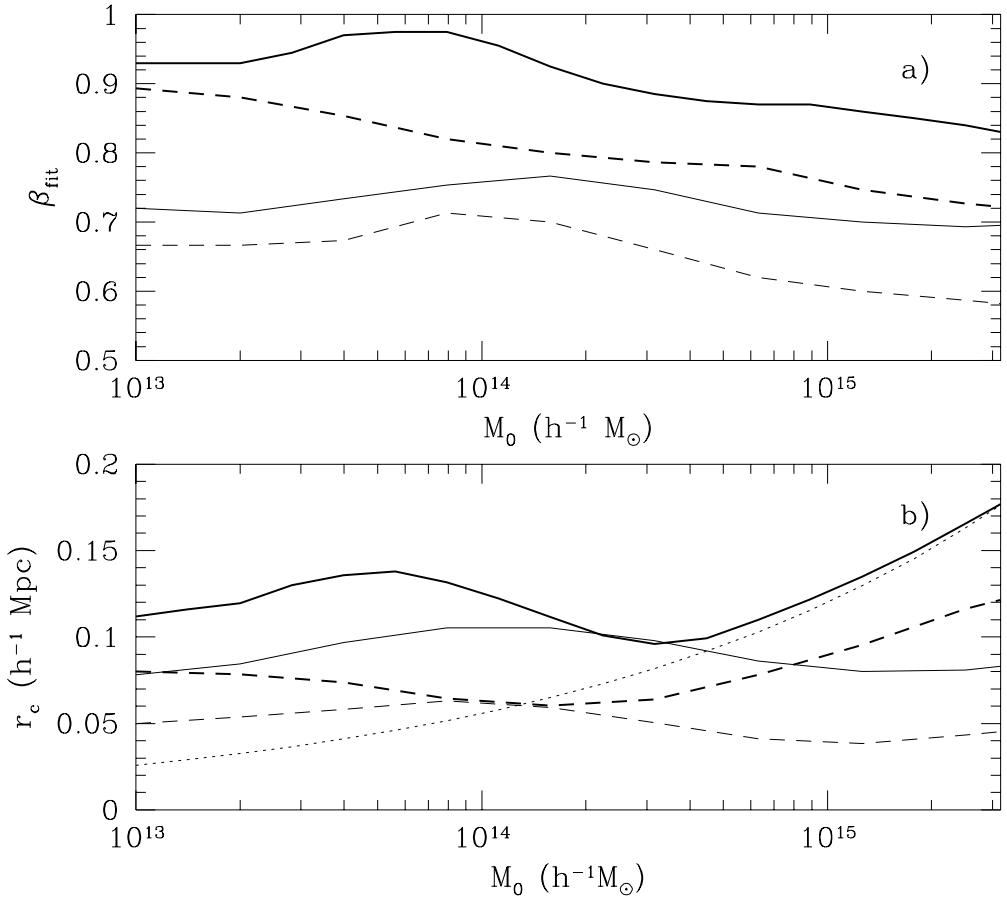


Fig. 8.— $-\beta_{fit}$ parameter and the core radius r_c as a function of the mass scale derived by fitting the predicted profiles with a beta model. The initial entropy is $K_* = 0.3 \times 10^{34} \text{ erg cm}^2 \text{ g}^{-5/3}$, constant with epoch, and the cooling is included. The thick lines refer to $z = 0$ and the thin lines to $z = 1$. The Λ CDM universe is shown with solid lines, while tCDM with dashed lines. A self-similar scaling radius ($r \propto M^{1/3}$) is shown with a dotted line for comparison.

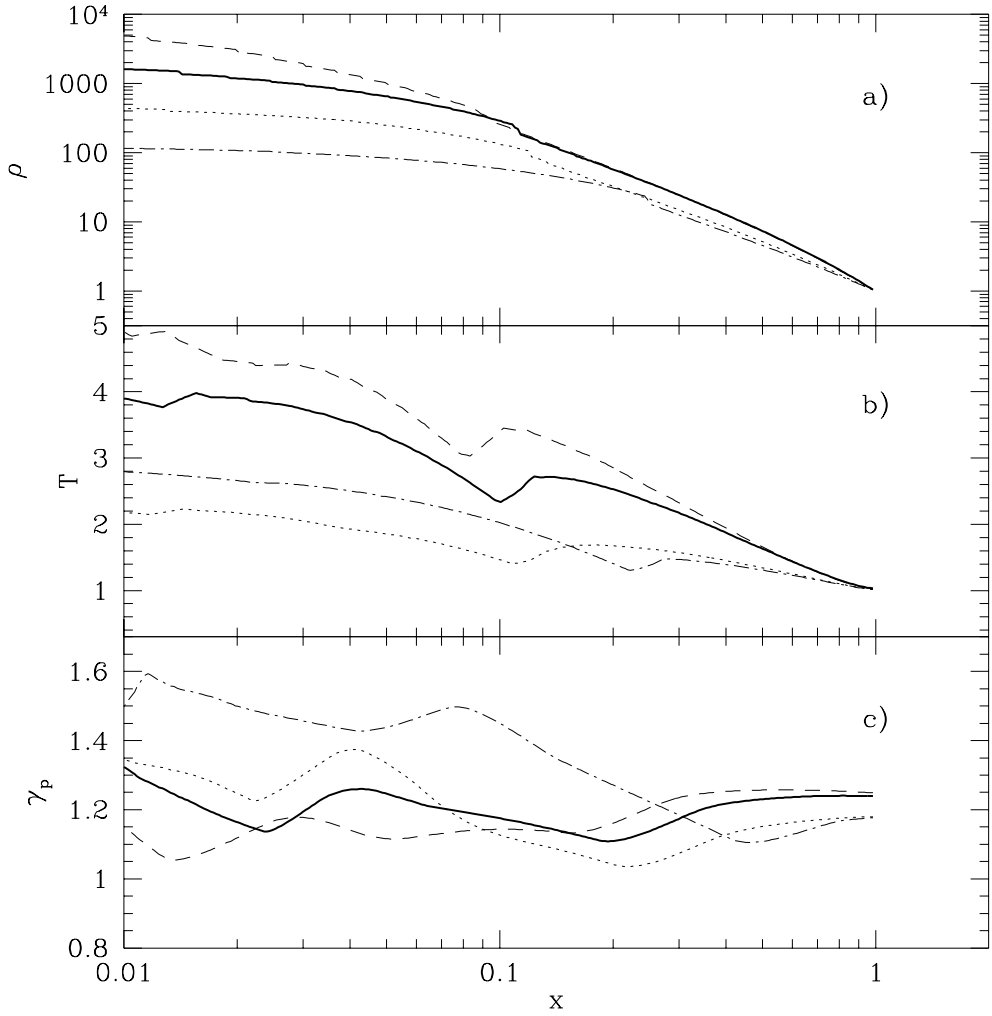


Fig. 9.— The heavy solid lines show the normalized density (panel a) and the normalized temperature (panel b) profiles for a cluster of $M = 0.6h^{-1}10^{15}M_{\odot}$ ($k_B T \simeq 5$ keV) in Λ CDM starting from the external adiabat $K_* = 0.4 \times 10^{34}$ erg cm 2 g $^{-5/3}$ (cooling is included). For comparison, we show the effect of changes in the dark matter profile from NFW to Moore et al. 1998 (dashed lines), of the epoch from $z = 0$ to $z = 1$ (dot-dashed lines) and of cosmology from Λ CDM to tCDM (dotted line). In panel c) the corresponding polytropic indexes γ_p are shown (averaged over $\Delta \log(x) = 0.3$).

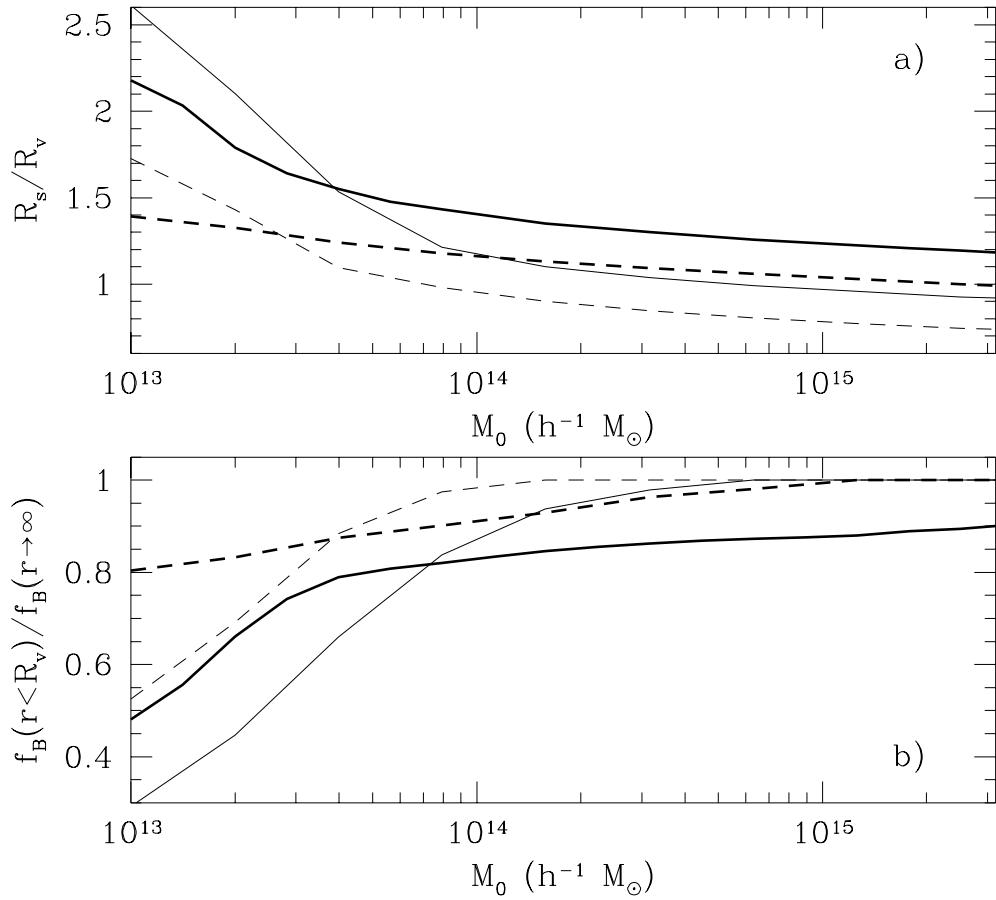


Fig. 10.— a) Ratio of the shock radius of the last accreted shell to the virial radius as a function of the mass scale; b) the baryonic fraction (with respect to the universal baryonic fraction) within the virial radius as a function of mass. The background entropy is $K_* = 0.3 \times 10^{34} \text{ erg cm}^2 \text{ g}^{-5/3}$ constant with epoch, and cooling is included. The thick lines refer to $z = 0$ and the thin to $z = 1$. The Λ CDM universe is shown with solid lines, while tCDM with dashed lines.

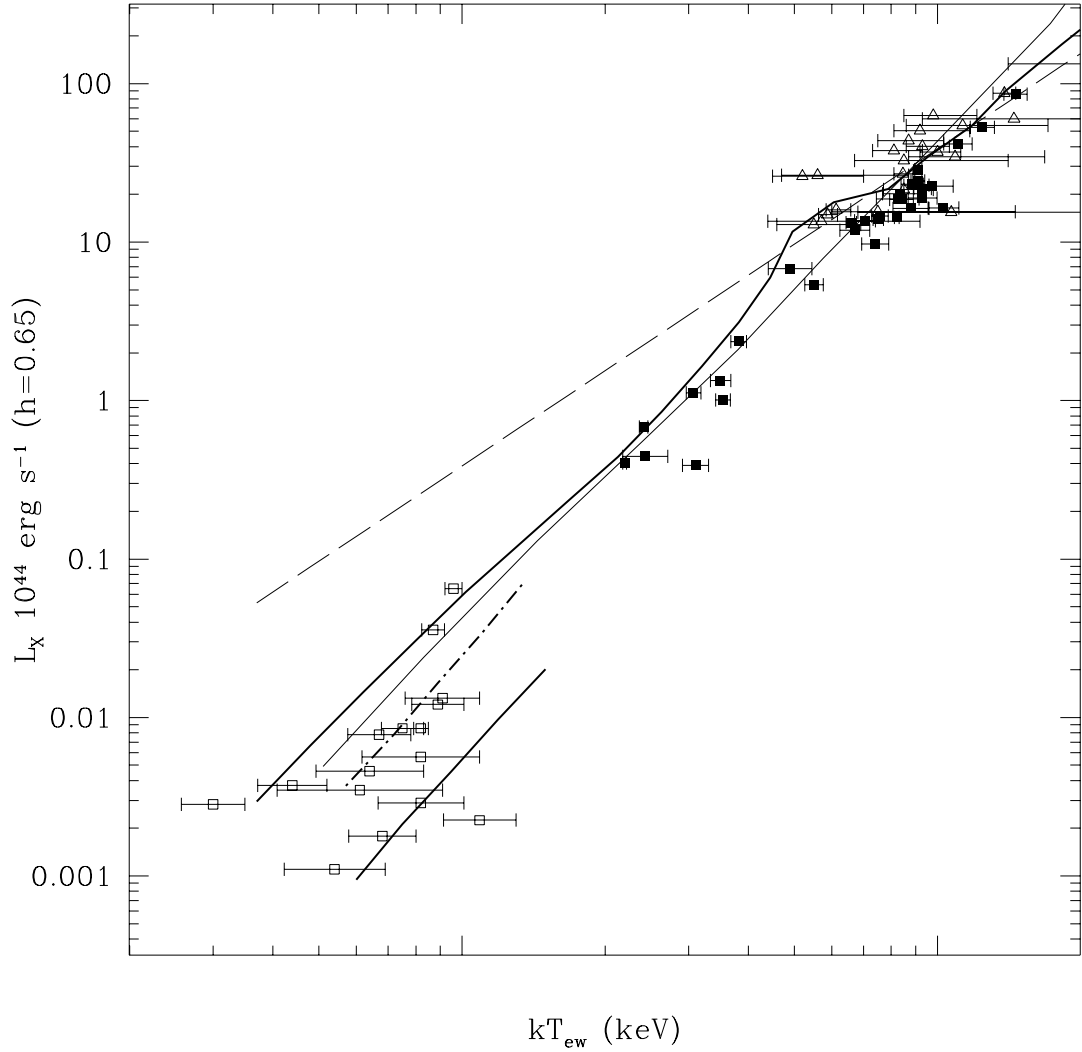


Fig. 11.— Relation between bolometric luminosity and emission weighted temperature in Λ CDM. The entropy background is $K_* = 0.3 \times 10^{34} \text{ erg cm}^2 \text{ g}^{-5/3}$ constant with epoch, and the cooling is included. Data are from Arnaud & Evrard (1999, filled squares), Allen & Fabian (1998, triangles) and Ponman et al. (1996, empty squares). The dashed lines refer to the self-similar case, while thick lines to $z_0 = 0$ and thin lines to $z_0 = 1$. The lower thick solid line for $k_B T \leq 1.5 \text{ keV}$ shows the $L-T$ relation at $z = 0$ defined within the projected radius of $100 h^{-1} \text{ kpc}$ as in Ponman et al. (1996). The lower thick dot-dashed line shows the same for $K_* = 0.2 \times 10^{34} \text{ erg cm}^2 \text{ g}^{-5/3}$.

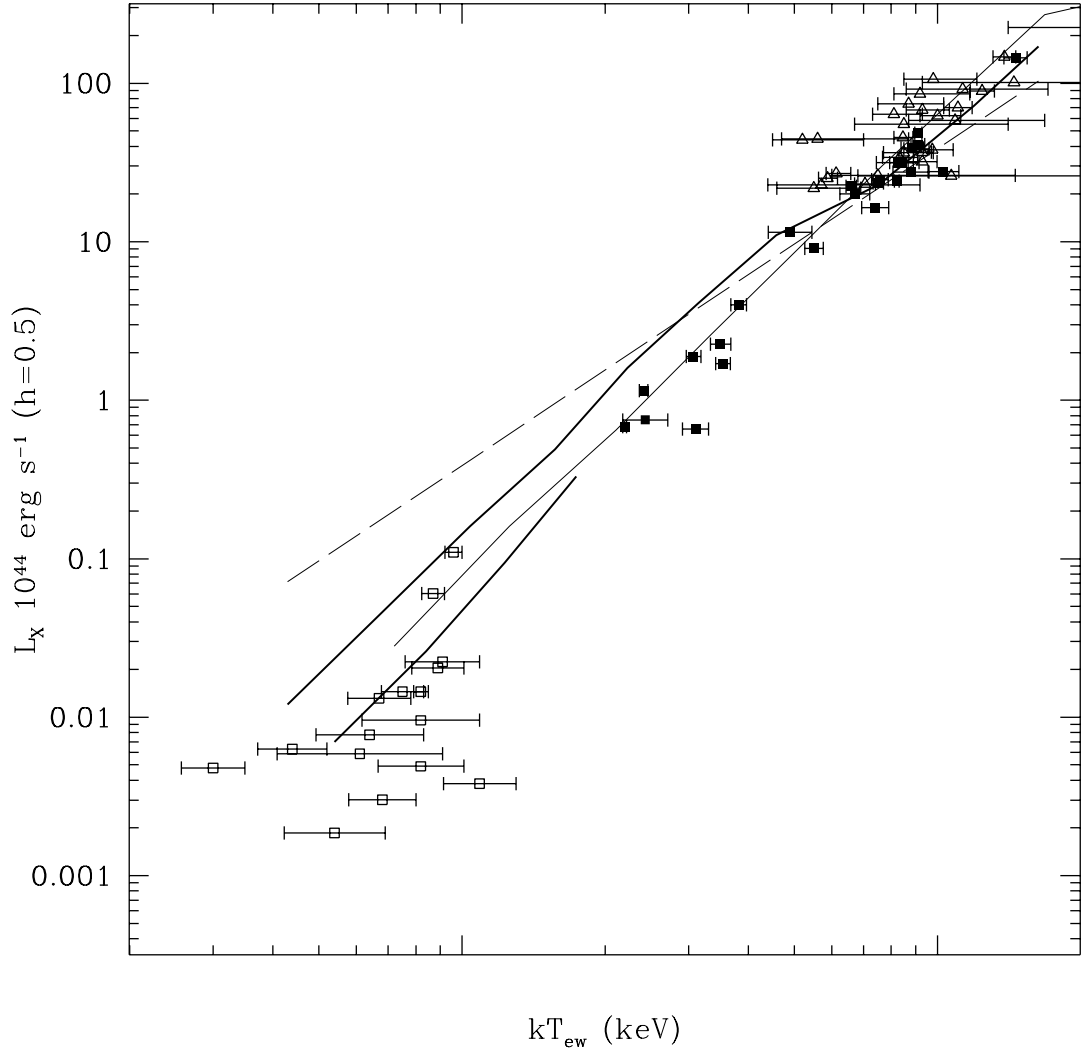


Fig. 12.— Relation between bolometric luminosity and emission weighted temperature in tCDM, notations as in Figure 11. Note that we are forced to use a baryonic density $\Omega_B = 0.04h^{-2}$, which is at least twice the value from standard nucleosynthesis constraints. The lower thick line for $k_B T \leq 1.5$ keV shows the $L-T$ relation at $z = 0$ defined within the projected radius of $100 h^{-1}$ kpc as in Ponman et al. (1996). Data as in Figure 11.

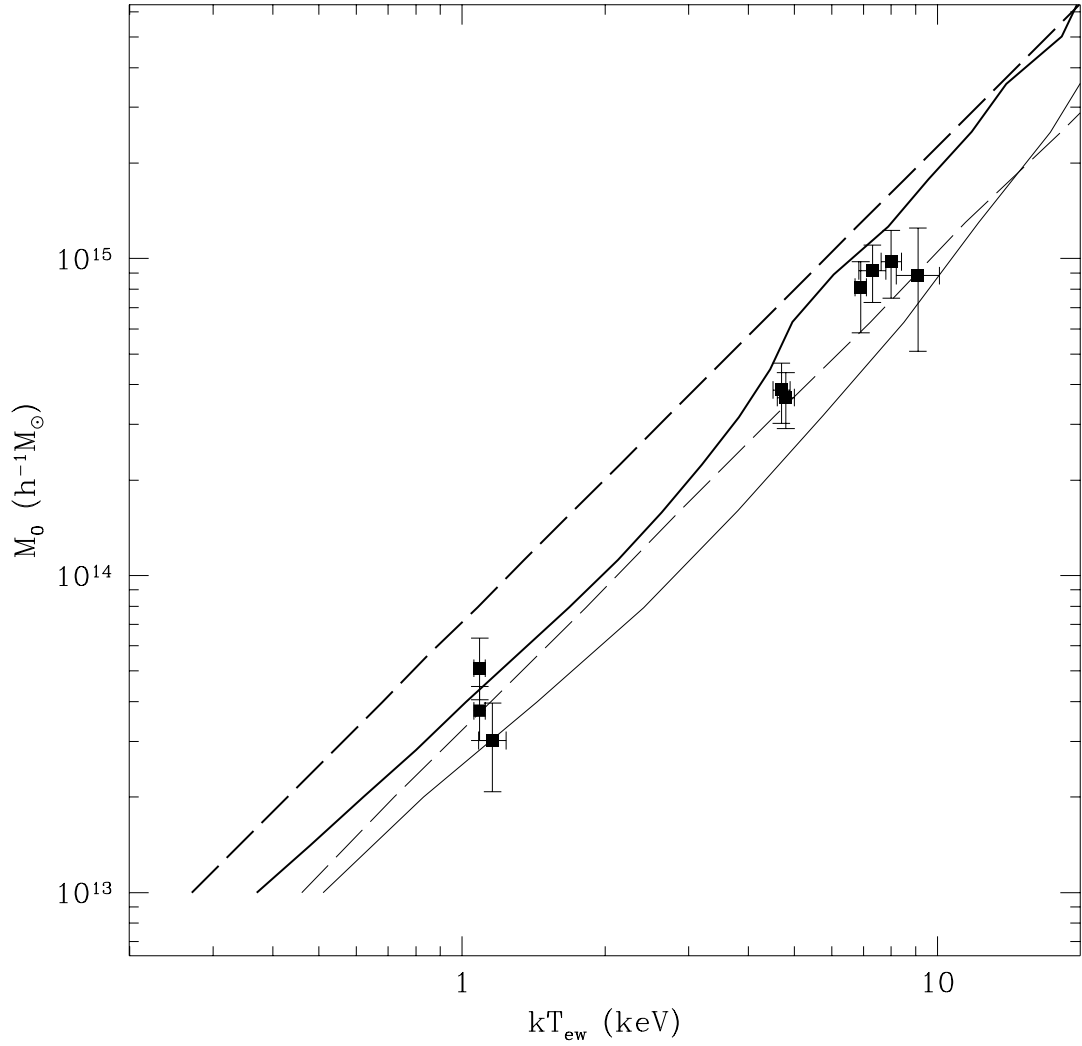


Fig. 13.— Relation between virial mass and emission weighted temperature in Λ CDM; data from Nevalainen, Markevitch & Forman (2000). The entropy background is $K_* = 0.3 \times 10^{34}$ erg cm 2 g $^{-5/3}$ constant with epoch, and the cooling is included. The dashed lines refer to the self-similar case, while thick lines to $z_0 = 0$ and thin lines to $z_0 = 1$. Note that the mass has been rescaled from M_{500} to the virial value using the corresponding NFW profile.

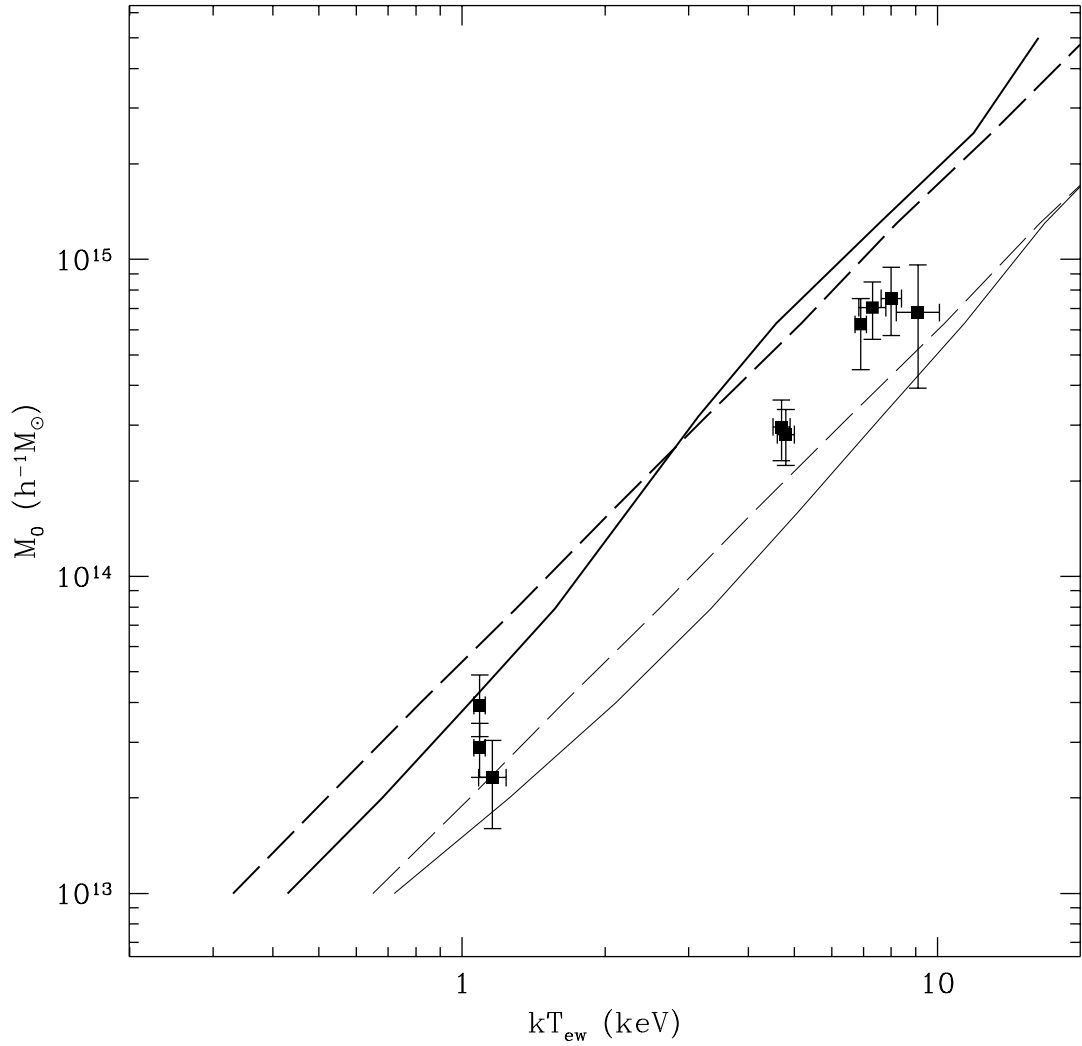


Fig. 14.— Relation between emission weighted temperature and virial mass in tCDM. The entropy background is $K_* = 0.3 \times 10^{34}$ erg cm 2 g $^{-5/3}$ constant with epoch, and the cooling is included. The dashed lines refer to the self-similar case, while thick lines to $z_0 = 0$ and thin lines to $z_0 = 1$. Data as in Figure 13.

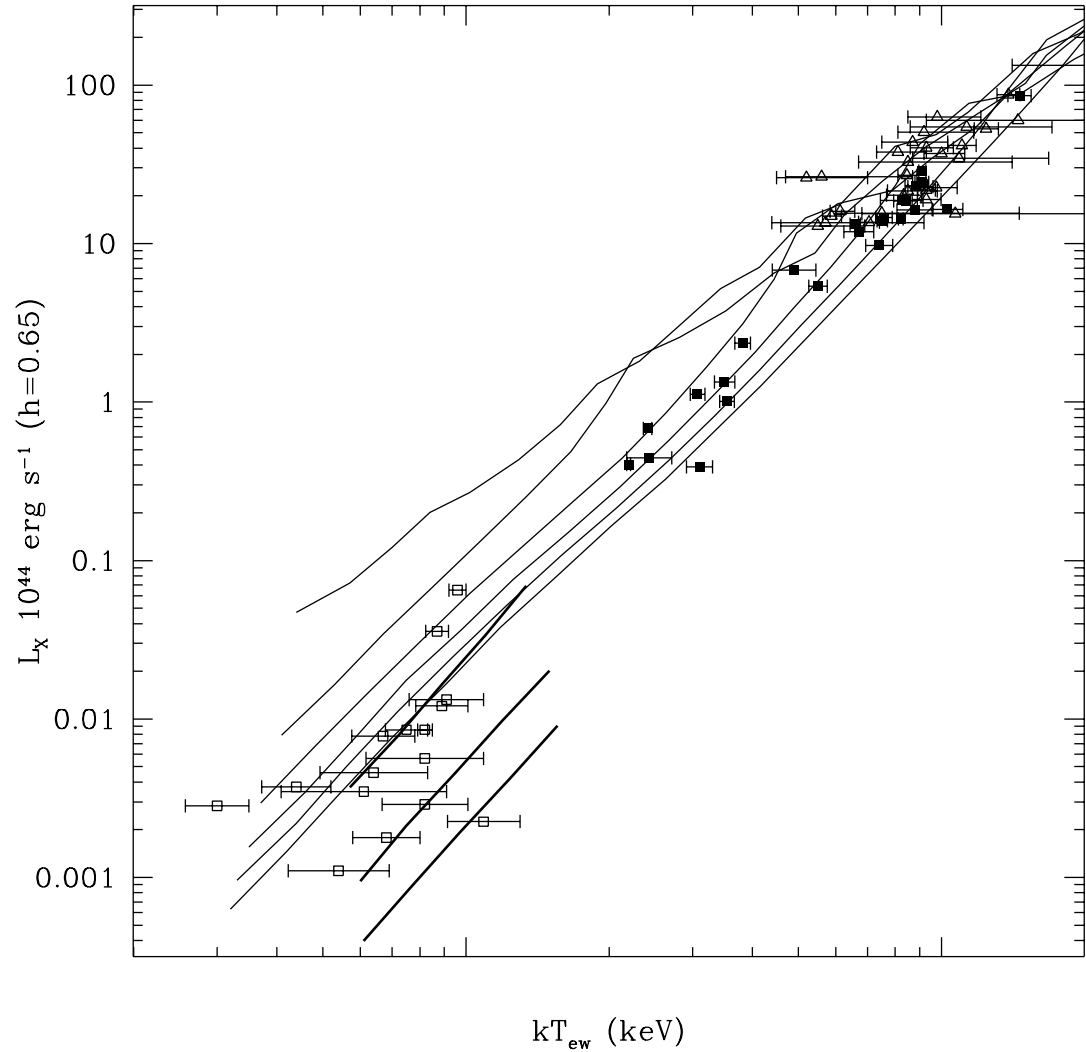


Fig. 15.— The thin lines show the $L-T$ relation at $z = 0$ in Λ CDM for different values of the initial adiabat (background entropy): from top to bottom $K_* = 0.1 - 0.2 - 0.3 - 0.4 - 0.5 - 0.6 \times 10^{34} \text{ erg cm}^2 \text{ g}^{-5/3}$. The thick segments shows the prediction limited to the inner $100 h^{-1} \text{ kpc}$ for $K_* = 0.2 - 0.3 - 0.4 \times 10^{34} \text{ erg cm}^2 \text{ g}^{-5/3}$. Data as in Figure 11.

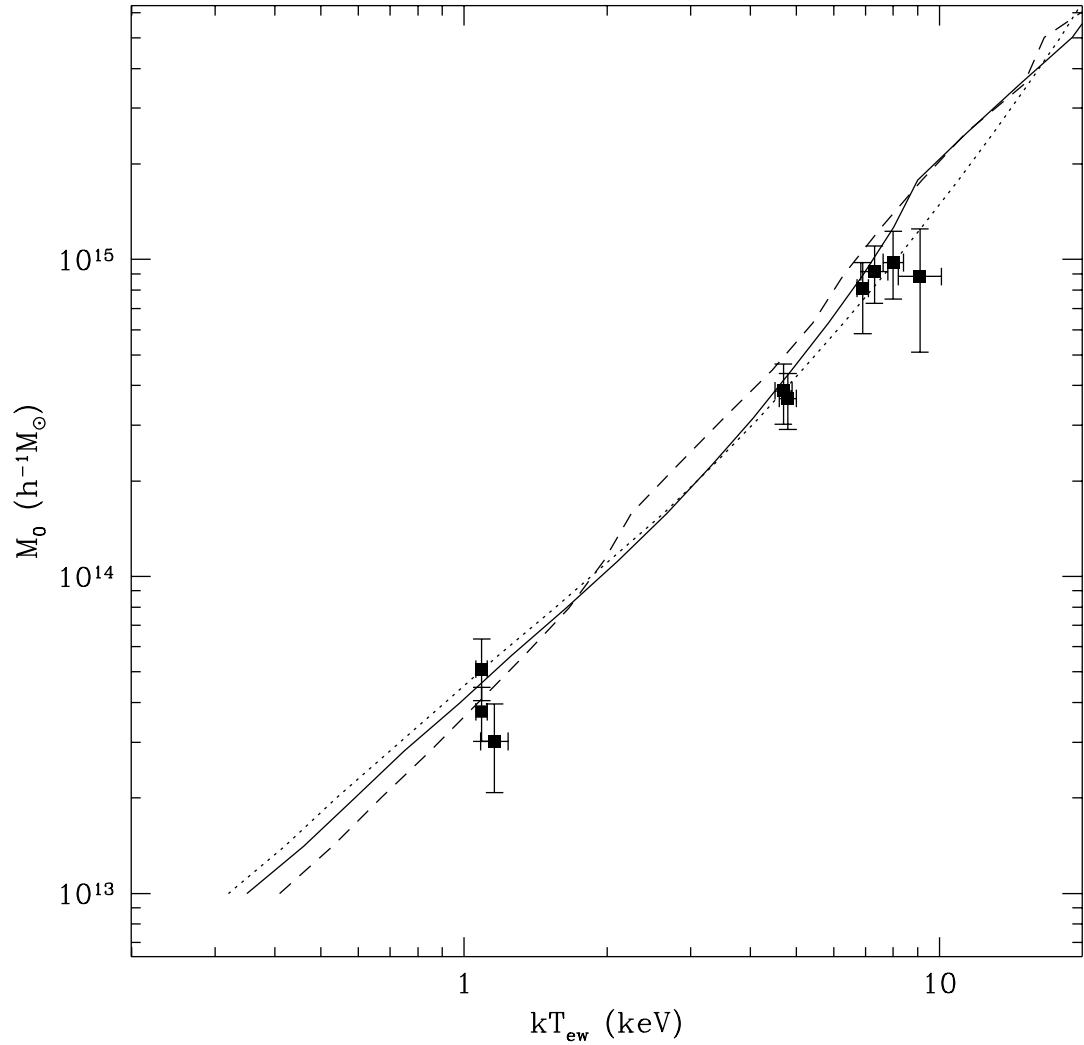


Fig. 16.— The M – T relation in Λ CDM for different values of the initial adiabat: $K_* = 0.2 - 0.4 - 0.6 \times 10^{34}$ erg cm 2 g $^{-5/3}$ (respectively dashed, solid and dotted lines). Data as in Figure 12.

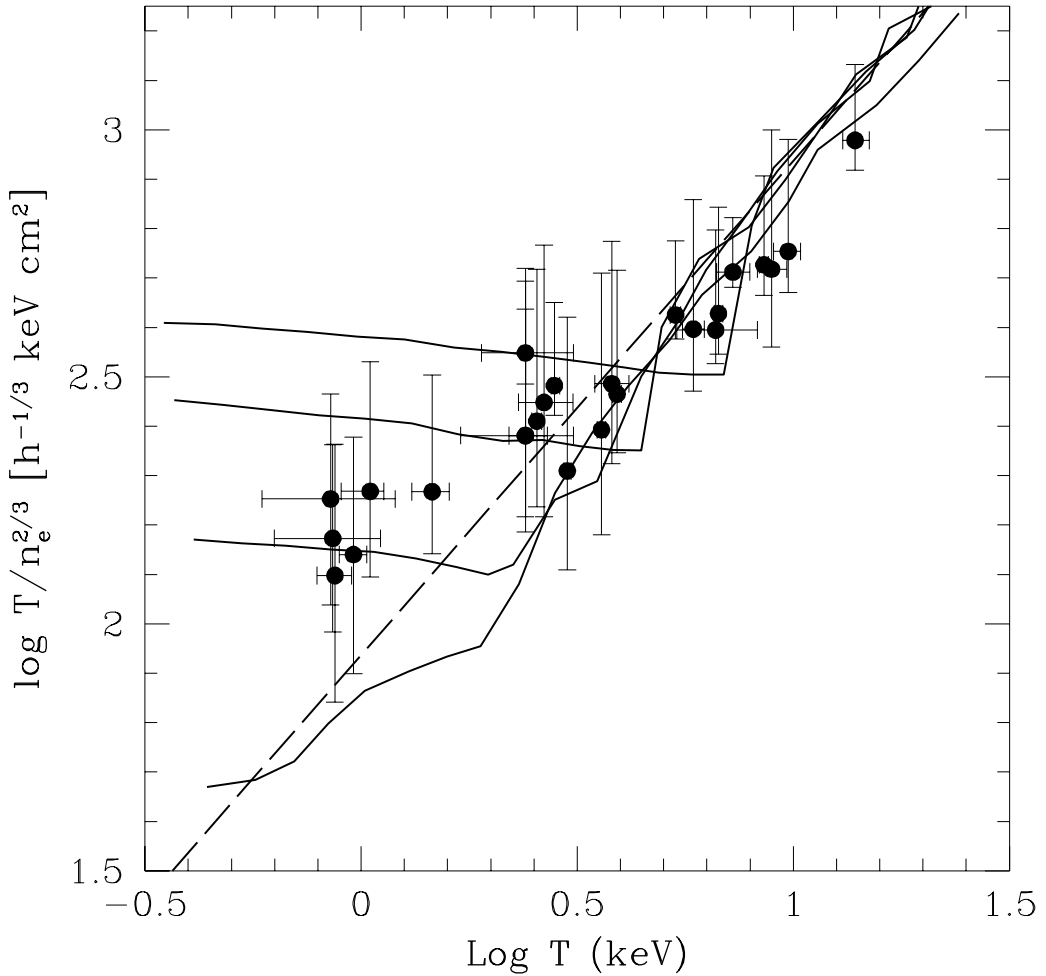


Fig. 17.— Relation between central entropy defined as in PCN as $T/n_e^{2/3}$ at $r = 0.1R_v$, as a function of the local temperature $T(r)$ for Λ CDM at redshift $z = 0$ for different value of the background entropy $K_* = 04. - 0.3 - 0.2 - 0.1 \times 10^{34} \text{ erg cm}^2 \text{ g}^{-5/3}$ (from top to bottom). Data are from PCN. The dashed line is the self similar case from N-body simulations, after PCN.

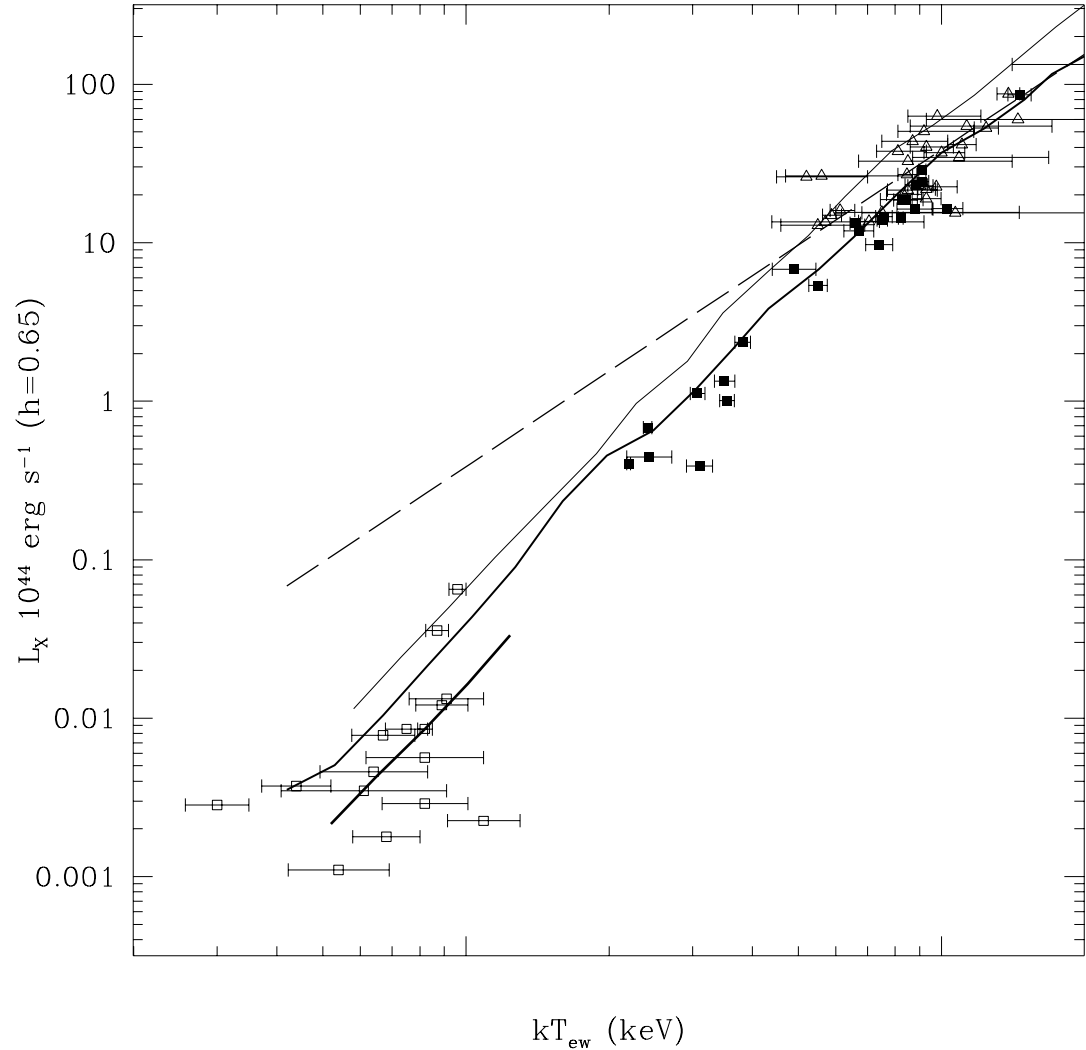


Fig. 18.— Relation between bolometric luminosity and emission weighted temperature in Λ CDM assuming an evolving entropy $K_* = 0.8(1+z)^{-1} \times 10^{34} \text{ erg cm}^2 \text{ g}^{-5/3}$. The thick line for $k_B T \leq 1.5 \text{ keV}$ shows the $L-T$ relation at $z = 0$ defined within the projected radius of $100 h^{-1} \text{ kpc}$ as in Ponman et al. (1996). The dashed lines refer to the self-similar case, while thick lines to $z_0 = 0$ and thin lines to $z_0 = 1$. Data as in Figure 11.

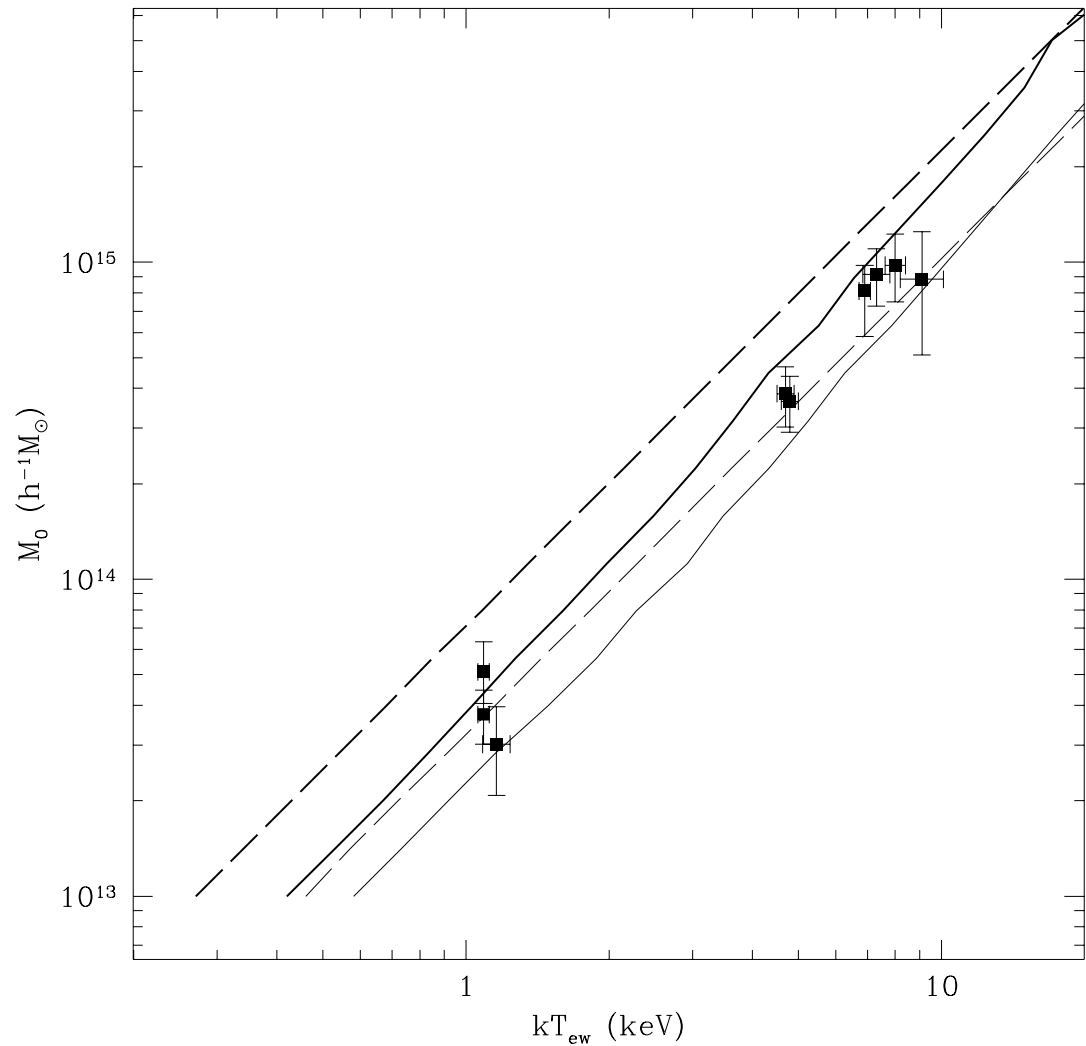


Fig. 19.— The M – T relation in Λ CDM assuming an evolving entropy $K_* = 0.8(1+z)^{-1} \times 10^{34}$ erg cm 2 g $^{-5/3}$. The dashed lines refer to the self-similar case, while thick lines to $z_0 = 0$ and thin lines to $z_0 = 1$. Data as in Figure 13.

Table 1. Cosmological parameters.

Model	Ω_M	Ω_Λ	h	n	σ_8
tCDM	1.0	0.0	0.5	0.8	0.55
Λ CDM	0.3	0.7	0.7	1.0	1.1

Note. — h is the Hubble constant in units of 100 km/sec/Mpc, σ_8 is the amplitude of the fluctuations at the scale of $8h^{-1}$ Mpc, and n is the primordial spectral index.

Table 2. Coefficients A and B for the mass histories of the main progenitors.

Model, z_0	$10^{12} h^{-1} M_\odot$	$10^{13} h^{-1} M_\odot$	$10^{14} h^{-1} M_\odot$	$10^{15} h^{-1} M_\odot$
tCDM, $z_0 = 0$	2.30 - 0.60	2.51 - 0.87	2.56 - 1.40	2.46 - 2.32
tCDM, $z_0 = 1$	3.02 - 1.78	3.20 - 2.36	2.82 - 3.32	1.76 - 5.05
Λ CDM, $z_0 = 0$	1.50 - 0.12	1.86 - 0.18	2.14 - 0.46	2.38 - 0.94
Λ CDM, $z_0 = 1$	1.92 - 0.88	2.38 - 1.14	2.48 - 1.82	2.20 - 2.94

Table 3. Parameters for the cooling function B4.

Metallicity	C_1	C_2	C_3
$0 Z_\odot$	1.19×10^{-4}	6.3×10^{-2}	1.9×10^{-2}
$0.1 Z_\odot$	2.8×10^{-3}	5.8×10^{-2}	4×10^{-2}
$0.3 Z_\odot$	8.6×10^{-3}	5.8×10^{-2}	6.3×10^{-2}

Note. — The units for C_1 are 10^{-22} erg cm 3 s $^{-1}$ keV $^{-\alpha}$; the units for C_2 are 10^{-22} erg cm 3 s $^{-1}$ keV $^{-\beta}$; the units for C_3 are 10^{-22} erg cm 3 s $^{-1}$.